

PAPER • OPEN ACCESS

Validation of 2D T_e and n_e measurements made with Helium imaging spectroscopy in the volume of the TCV divertor

To cite this article: B.L. Linehan *et al* 2023 *Nucl. Fusion* **63** 036021

View the [article online](#) for updates and enhancements.

You may also like

- [Trends in runaway electron plateau partial recombination by massive H₂ or D₂ injection in DIII-D and JET and first extrapolations to ITER and SPARC](#)
E.M. Hollmann, L. Baylor, A. Boboc et al.
- [Magnetic island formation and rotation braking induced by low-Z impurity penetration in an EAST plasma](#)
Shiyong Zeng, Ping Zhu, Ruijie Zhou et al.
- [Simulations of nonlinear interaction between beta-induced Alfvén eigenmode and tearing mode](#)
Sizhe Duan, Xiaogang Wang, Huishan Cai et al.

Validation of 2D T_e and n_e measurements made with Helium imaging spectroscopy in the volume of the TCV divertor

B.L. Linehan^{1,*} , A. Perek^{2,3} , B.P. Duval² , F. Bagnato² , P. Blanchard², C. Colandrea², H. De Oliveira², O. Février² , E. Flom⁴ , S. Gorno² , M. Goto⁵ , E. Marmar¹, L. Martinelli² , A. Mathews¹ , J. Muñoz-Burgos⁷ , D. Mykytchuk², N. Offeddu² , D.S. Oliveira² , H. Reimerdes² , D. Reiter⁸ , O. Schmitz⁴ , J.L. Terry¹ , C. Theiler² , C.K. Tsui⁶ , B. Vincent² , T. Wijkamp³ , C. Wüthrich² , W. Zholobenko⁹  and the TCV Team^a

¹ Massachusetts Institute of Technology, Cambridge, MA, United States of America

² Ecole Polytechnique Fédérale de Lausanne (EPFL), Swiss Plasma Center (SPC), CH-1015 Lausanne, Switzerland

³ DIFFER-Dutch Institute for Fundamental Energy Research, De Zaale 20, 5612 AJ Eindhoven, Netherlands

⁴ University of Wisconsin Madison, 702 West Johnson Street Madison, Madison, WI 53715, United States of America

⁵ National Institute for Fusion Science, Toki 509-5292, Japan

⁶ Center for Energy Research (CER), University of California-San Diego (UCSD), La Jolla, CA 92093 United States of America

⁷ Astro Fusion Spectre LLC, San Diego, CA, 92127, United States of America

⁸ Institut für Laser- und Plasmaphysik, Heinrich-Heine-Universität, Düsseldorf 40225, Deutschland

⁹ Max-Planck-Institut für Plasmaphysik, Garching 85748, Deutschland

E-mail: blinehan@mit.edu

Received 24 October 2022, revised 13 January 2023

Accepted for publication 24 January 2023

Published 10 February 2023



Abstract

Multi-spectral imaging of helium atomic emission (HeMSI) has been used to create 2D poloidal maps of T_e and n_e in TCV's divertor. To achieve these measurements, TCV's MANTIS multispectral cameras (Perek *et al* 2019 *Rev. Sci. Instrum.* **90** 123514) simultaneously imaged four He I lines (two singlet and two triplet) and a He II line (468 nm) from passively present He and He⁺. The images, which were absolutely calibrated and covered the whole divertor region, were inverted through the assumption of toroidal symmetry to create emissivity profiles and, consequently, line-ratio profiles. A collisional-radiative model (CRM) was applied to the line-ratio profiles to produce 2D poloidal maps of T_e and n_e . The collisional-radiative modeling was accomplished with the Goto helium CRM code (Zholobenko *et al* 2018 *Nucl. Fusion* **58** 126006, Zholobenko *et al* 2018 *Technical Report*, Goto 2003 *J. Quant. Spectrosc. Radiat. Transfer* **76** 331–44) which accounts for electron-impact excitation (EIE) and deexcitation, and electron-ion recombination (EIR) with He⁺. The HeMSI T_e and n_e measurements were

^a See Reimerdes *et al* 2022 (<https://doi.org/10.1088/1741-4326/ac369b>) for the TCV Team.

* Author to whom any correspondence should be addressed.



Original Content from this work may be used under the terms of the [Creative Commons Attribution 4.0 licence](https://creativecommons.org/licenses/by/4.0/). Any further distribution of this work must maintain attribution to the author(s) and the title of the work, journal citation and DOI.

compared with co-local Thomson scattering measurements. The two sets of measurements exhibited good agreement for ionizing plasmas: ($5\text{ eV} \leq T_e \leq 60\text{ eV}$, and $2 \times 10^{18}\text{ m}^{-3} \leq n_e \leq 3 \times 10^{19}\text{ m}^{-3}$) in the case of majority helium plasmas, and ($10\text{ eV} \leq T_e \leq 40\text{ eV}$, $2 \times 10^{18}\text{ m}^{-3} \leq n_e \leq 3 \times 10^{19}\text{ m}^{-3}$) in the case of majority deuterium plasmas. However, there were instances where HeMSI measurements diverged from Thomson scattering. When $T_e \leq 10\text{ eV}$ in majority deuterium plasmas, HeMSI deduced inaccurately high values of T_e . This disagreement cannot be rectified within the CRM's EIE and EIR framework. Second, on sporadic occasions within the private flux region, HeMSI produced erroneously high measurements of n_e . Multi-spectral imaging of Helium emission has been demonstrated to produce accurate 2D poloidal maps of T_e and n_e within the divertor of a tokamak for plasma conditions relevant to contemporary divertor studies.

Keywords: scrape-off layer, multi-spectral imaging, TCV, helium collisional radiative modeling, plasma boundary physics, tokamak divertor, tokamak diagnostics

(Some figures may appear in colour only in the online journal)

1. Introduction

Solving the plasma exhaust problem is a prerequisite for future commercial tokamak reactors. Research dedicated to advancing theoretical understanding and computational modeling of the boundary of a diverted tokamak plasma continues towards this goal ([1] and references therein). Critical to such progress are local measurements of T_e and n_e in the volume of the scrape-off layer of present-day experiments. However, various constraints limit the spatial coverage of such measurements. Generally, the diagnostic coverage of T_e and n_e in the plasma boundary is limited to a relatively sparse collection of Thomson scattering or Langmuir probe measurements. Thomson scattering measurements are confined to the one-dimensional path of their lasers, and Langmuir probe measurements (when non-invasive) occur at the surface of the vessel. Consequently, the majority of the boundary volume lacks diagnostic coverage. This is particularly problematic for divertor experiments at the tokamak à configuration variable (TCV)[2–5]. Diagnostic coverage cannot be tuned to an optimal coverage for all experiments because of the diversity of magnetic geometries explored and the large divertor volume (see figure 1).

These constraints motivate the ongoing development of imaging techniques at TCV with the high-resolution multi-spectral cameras deemed the Multispectral Advanced Narrowband Tokamak Imaging System (MANTIS) diagnostics [6]. These MANTIS cameras employ a polychromator design allowing them to image up to ten individual spectral lines simultaneously over the same tangential view of the chamber. The images are absolutely calibrated, and by assuming toroidal symmetry, the images are tomographically inverted to create 2D poloidal emissivity maps. Analysis of the emissivity maps of the several Balmer lines observed by MANTIS was reported on previously in Perek [7] and Perek [8].

This paper describes the measurement of 2D poloidal profiles of T_e and n_e via multi-spectral imaging of helium lines (HeMSI) at TCV and the experiments performed to validate the profiles against co-local divertor Thomson scattering measurements. To perform these measurements, the absolute brightnesses of 4 He I lines, 728.2 nm ($3^1S \rightarrow 2^1P$),

667.8 nm ($3^1D \rightarrow 2^1P$), 706.5 nm ($3^3S \rightarrow 2^3P$) and 587.6 nm ($3^3D \rightarrow 2^3P$), and a He II line, 468 nm ($4 \rightarrow 3$) were simultaneously imaged with sightlines covering the entire divertor cross-section. These images were then inverted into poloidal emissivity profiles. Then, the ratios of emissivities at each point in the poloidal grid were independently regressed to T_e and n_e values using a collisional-radiative model (CRM) for He. The CRM accounted for electron-impact excitation (EIE) and deexcitation and electron-ion recombination (EIR) with He^+ . The atomic rates used in the CRM were taken from the *Goto* He CRM (G-CRM)[9–11].

The application of helium line-ratios as a T_e and n_e diagnostic was first proposed by Cunningham in 1955 [12]. Helium line-ratio spectroscopy (HLRS) has since become an effective plasma diagnostic and has been utilized in multiple plasma experiments including: AUG [13, 14], **Magnum** [15], **PISCES-A** [16], **W7X** [9, 10], **TEXTOR** [17], **LHD** [18], **MAP-II** [19, 20], **H-1** [21], **TJ-II** [22], **MAST** [23], **Nagdis-II** [24], **RFX** [25], **COMPASS** [26], **JT-60** [27], and **JET** [28]. The work presented here is innovative in that it was the first application of HLRS in a tokamak which incorporated 2D poloidal emissivity profiles. Traditional HLRS methodologies in tokamaks have utilized a localized He gas puff. The advantages of the gas puff methodology are that it does not require the inversion of images and recombination processes can typically be ignored. However, the methodology is limited in its spatial coverage and is inherently perturbative. While HeMSI requires image inversions and consideration of recombination processes, this innovative approach produces 2D T_e and n_e profiles with unprecedented spatial coverage. Furthermore, HeMSI requires viewing multiple lines simultaneously with sufficient resolution to permit inversion. Thus, HeMSI has only now been made feasible for a tokamak experiment with the introduction of the MANTIS diagnostics at TCV.

Excluding a few exceptions to be noted, HeMSI was shown in the experiments to produce good agreement with Thomson scattering for ionizing plasmas: $5\text{ eV} \leq T_e \leq 60\text{ eV}$ and $2 \times 10^{18}\text{ m}^{-3} \leq n_e \leq 3 \times 10^{19}\text{ m}^{-3}$ in majority helium plasmas, and $10\text{ eV} \leq T_e \leq 40\text{ eV}$ and $2 \times 10^{18}\text{ m}^{-3} \leq n_e \leq 3 \times 10^{19}\text{ m}^{-3}$ in majority deuterium

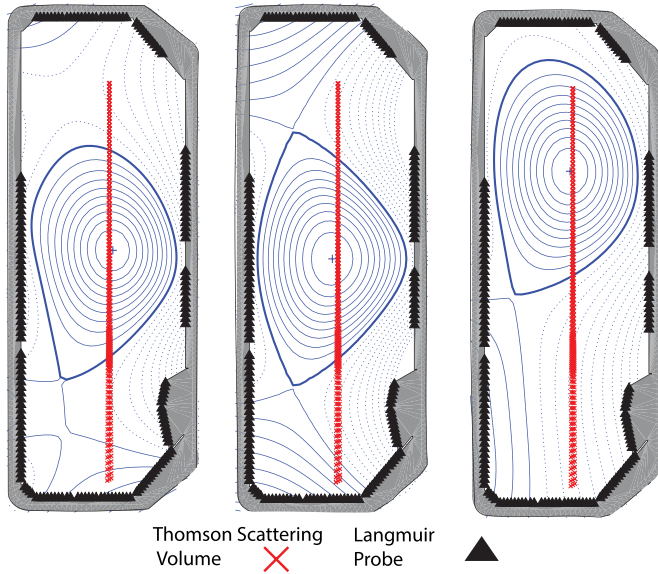


Figure 1. Magnetic reconstructions from three TCV discharges. They illustrate the wide-range of magnetic geometries explored at TCV and the amount of plasma volume in the boundary that goes without T_e and n_e diagnostic coverage.

plasmas. For deuterium plasmas with $T_e < 10\text{eV}$, HeMSI significantly overestimated T_e according to Thomson scattering. This deviation from agreement was consistent with reports from other helium–hydrogen plasma experiments [19, 29–33], and suggests that the CRM is omitting key processes in this regime. Lastly, HeMSI measurements intermittently diverged from those of Thomson scattering in the private flux region, and the root of this sporadic disagreement is not currently known.

This paper is organized into the following sections. Section 2 gives an overview of helium collisional-radiative modeling, how line-ratios are mapped to T_e and n_e measurements, and the sources of atomic rates. Section 3 details the MANTIS diagnostics. Section 4 provides a qualitative description of the He, He II and C III images observed by MANTIS at TCV. The C III line is included as it will be used to confirm that the plasma is an ionizing plasma in the future when HeMSI is used apart from Thomson scattering. Section 5 describes the series of discharges used to validate HeMSI measurements against Thomson scattering measurements. Section 6 explains how the data from Thomson scattering and HeMSI were consolidated in order to facilitate their comparison and their presentation in this work. Section 7 presents and discusses the HeMSI and Thomson scattering measurements and the results of their comparison. Finally, section 8 summarizes the results and concludes the paper.

2. Helium CRM

A CRM describes the evolution of atomic or molecular state populations within a background plasma. In diagnostic applications, CRMs are used to forward-model atomic emissions

from plasma parameters, including T_e and n_e , so that they may be determined by fitting the predictions to spectroscopic measurements. Collisional-radiative modeling originated in Bates [34], and has since been thoroughly described in several works. The general theory of CRMs is presented in Fujimoto [35] and Summers *et al* [36]. The original derivation of metastable resolved He CRMs was first given in Fujimoto [37]. More recent explanations of the helium CRMs can be found in Goto [11], Muñoz-Burgos *et al* [38], and Zholobenko [9, 10].

Quantitatively, a CRM is a system of first-order differential rate equations. The helium collisional model utilized in this work accounts for: radiative decay ($A_{i \rightarrow j}$), EIE and deexcitation ($q_{i \rightarrow j}^e$), electron impact ionization (S_i^e), three-body recombination (α_i), radiative recombination (β_i), and dielectronic recombination (β_i^d). The three recombination processes will be referred to collectively as electron–ion recombination (EIR). The system of equations defining the He CRM is given in equation (1), and a description of each term in equation (1) is given in table 1.

$$\frac{dn_i}{dt} = \sum_{j \neq i} (A_{j \rightarrow i} + n_e q_{j \rightarrow i}^e) n_j - \left(\sum_{j < i} A_{i \rightarrow j} + \sum_{j \neq i} n_e q_{i \rightarrow j}^e + n_e S_i^e \right) n_i + n_{\text{He}^+} n_e (\alpha_i + \beta_i + \beta_i^d). \quad (1)$$

A key result of collisional-radiative modeling is that the populations of many excited states can be approximated as residing in a quasi-static equilibrium (QSE) with the background plasma, i.e. $\frac{dn_i}{dt} = 0$. In regards to equation (1), QSE means that the population of such an excited state becomes solely a function of T_e , n_e , n_{He^+} , and the populations of ground and metastable helium states. The timescale, relaxation time, for an atomic state of helium to reach QSE is given by [35]:

$$\tau_{\text{relax}}^i = \frac{1}{(\sum_{j < i} A_{i \rightarrow j} + \sum_{j \neq i} n_e q_{i \rightarrow j}^e + n_e S_i^e)}. \quad (2)$$

In this work, all excited states including metastables will be assumed to be in QSE. The metastable state 2^3S cannot decay through a radiative dipole transition and is the slowest to relax. Therefore, τ_{relax} , which is defined here as the relaxation time for all states, is given by

$$\tau_{\text{relax}} \equiv \tau_{\text{relax}}^{2^3S} = \frac{1}{(n_e q_{2^3S \rightarrow j}^e + n_e S_{2^3S}^e)}. \quad (3)$$

In regards to HeMSI and following from equation (3), the criterion for QSE to be applicable to neutral helium traversing the divertor is:

$$\frac{\lambda_{(T_e, n_e)}^{\text{pol}}}{v_{\text{He}}} \ll \tau_{\text{relax}} \quad (4)$$

where $\lambda_{(T_e, n_e)}^{\text{pol}}$ is the length scale in the poloidal plane over which T_e and n_e vary, and v_{He} is the velocity of the helium atoms. In this work, helium atoms are assumed to be at the temperature of the walls, $\approx 300\text{K}$. Figure 2(a) depicts the relaxation time and the average distance traveled in the poloidal plane by helium atoms at 300K in one τ_{relax} interval. In the

Table 1. Description of parameters included in equation (1).

n_e	Electron density
T_e	Electron temperature
$n_{\text{He}, \text{He}^+}$	Neutral He, or He^+ density
n_i	Density of the i th He atomic state
$q_{i \rightarrow j}^e(T_e)$	Electron impact (de-)excitation rate coefficient from n_i to n_j
$S_i^e(T_e)$	Electron impact ionization rate coefficient from n_i to He^+
$\alpha_i(T_e, n_e), \beta_i(T_e), \beta_i^d(T_e)$	Three-body, radiative, and dielectronic recombination rate coefficients
$A_{i \rightarrow j}$	Einstein spontaneous emission coefficients ($A_{i \rightarrow j} = 0$ for $i \geq j$)

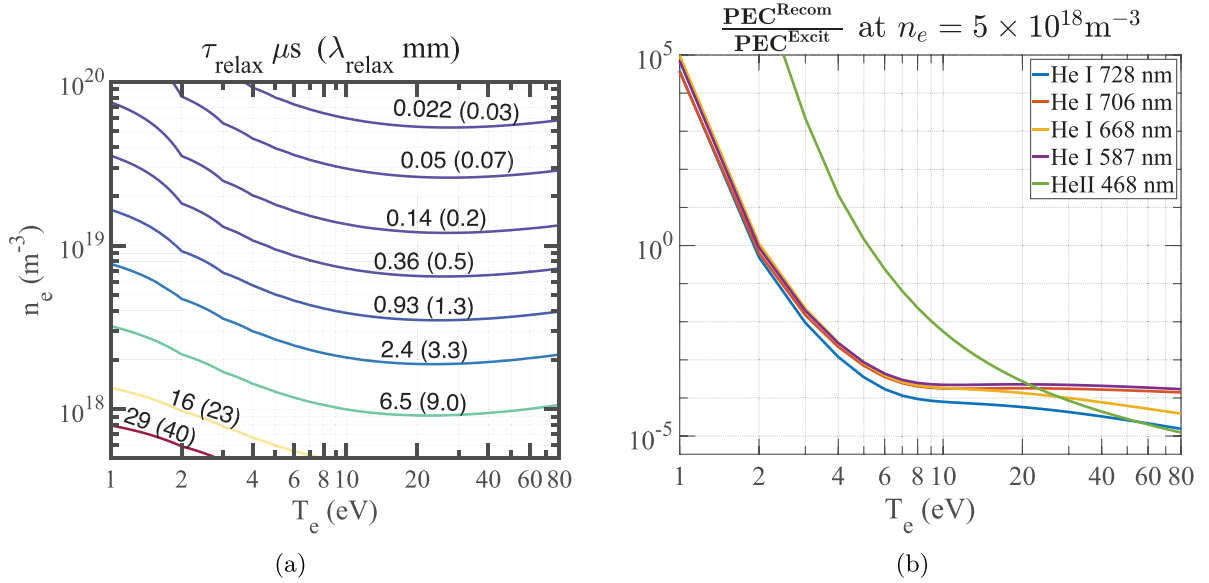


Figure 2. (a): Relaxation time, τ_{relax} , and the average distance traveled in the poloidal plane during that time, λ_{relax} , by neutral helium atoms at 300K and in a 1.4 T magnetic field. (b): Ratio of $\text{PEC}_{\text{Recom}}$ to $\text{PEC}_{\text{Excit}}$ as a function of T_e at $5 \times 10^{18} \text{m}^{-3}$.

context of TCV, $\lambda_{(T_e, n_e)}^{\text{pol}} \approx 2 \text{ cm}$, and $n_e > 2 \times 10^{18} \text{m}^{-3}$ along the leg of an L-mode plasma. Therefore, looking at figure 2(a), an assumption of QSE for the metastable helium states is justified for the plasmas analyzed in this work.

Setting $\frac{dn_i}{dt} = 0$ for all but the 1^1S state, equation (1) simplifies to:

$$n(p) = r_0(p)n_e n_{\text{He}^+} + r_1(p)n_e n(1^1S) \quad (5)$$

where p indexes an excited state of helium, the $r_0(p)$ and $r_1(p)$ are coefficients determined by T_e and n_e , and $n(X)$ denotes the number density of species X .

The emissivity produced from the $n_i \rightarrow n_j$ transition (with units $\frac{\text{photons}}{\text{s} \cdot \text{m}^3}$) is given by:

$$\epsilon_{i \rightarrow j}(t) = A_{i \rightarrow j} n_i(t). \quad (6)$$

Combining equations (5) and (6) yields:

$$\epsilon_{i \rightarrow j}^{\text{He}} = A_{i \rightarrow j} r_1(i) n_{\text{He}(1^1S)} n_e + A_{i \rightarrow j} r_0(i) n_{\text{He}^+} n_e. \quad (7)$$

Adjusting the notation going forward, the $A_{ij}r(i)$ terms are relabeled as photon emissivity coefficients (PECs) in accordance with the terminology of Summers *et al* [36], and it is assumed that $n_{\text{He}} \approx n_{\text{He}(1^1S)}$. Thus, equation (7) becomes:

$$\epsilon_{i \rightarrow j}^{\text{He}} = n_{\text{He}} n_e \text{PEC}_{\text{Excit}}^{i \rightarrow j} + n_{(\text{He}^+)} n_e \text{PEC}_{\text{Recom}}^{i \rightarrow j}. \quad (8)$$

Equation (8) shows that Helium emission is driven by two processes, EIE which corresponds to the $n_{\text{He}} n_e \text{PEC}_{\text{Excit}}^{i \rightarrow j}$ term and EIR which corresponds to the $n_{(\text{He}^+)} n_e \text{PEC}_{\text{Recom}}^{i \rightarrow j}$ term. In this work, it will be assumed the EIE emission dominates. Motivation for this assumption is seen in figure 2(b) wherein it can be seen that:

$$\frac{\text{PEC}_{\text{Recom}}}{\text{PEC}_{\text{Excit}}} \ll 1 \quad (T_e > 2 \text{ eV}). \quad (9)$$

It is assumed in this work that n_{He^+} is not large enough to overcome the disparity between $\text{PEC}_{\text{Recom}}$ and $\text{PEC}_{\text{Excit}}$. Therefore, the emissivity of He I line can be approximated as:

$$\epsilon_{i \rightarrow j}^{\text{He}} \approx n_{\text{He}} n_e \text{PEC}_{\text{Excit}}^{i \rightarrow j}. \quad (10)$$

2.1. Fitting data to forward model

Measurements of T_e and n_e are inferred by matching the observed relative intensities of He I lines to CRM predictions. Using equation (10), the line-ratios can be expressed as

$$r_{ab} = \frac{\epsilon_a}{\epsilon_b} \approx \frac{\text{PEC}_{\text{Excit}}^a}{\text{PEC}_{\text{Excit}}^b}. \quad (11)$$

Table 2. References to the two CRMs and the rates they employ.

	G-CRM	A-CRM
References describing CRM	[9–11]	[38]
$A_{i \rightarrow j}$ source	[39]	[40]
$q_{i \rightarrow j}^e(T_e)$ source	[9, 10, 41]	[42]
$S_i^e(T_e)$ source	[9, 10, 41]	[41, 43]
$\alpha_i(T_e, n_e), \beta_i(T_e), \beta_i^d(T_e)$ source	See reference within [37]	[42, 44]
Includes effects of magnetic field	Yes	No

In these HeMSI validation experiments, 4 He I lines, 728 nm, 706 nm, 668 nm, and 587 nm were observed. The fitted T_e and n_e were determined by performing a least squares regression between the measured He I line ratios and the predictions of the CRM being scanned over the T_e and n_e parameter space, i.e.:

$$(T_e, n_e)_{\text{fit}} = \arg \min \sum_i \left(1 - \frac{r_i^{\text{obs}}}{r_i^{\text{model}}(T_e, n_e)} \right)^2. \quad (12)$$

2.2. Sources of atomic rates

The efficacy of collisional radiative modeling is constrained by the accuracy of the atomic rates. Two different helium CRM codes which utilize different sources of atomic data were used in the analysis of the HeMSI measurements. The first code [9–11] has been dubbed the Goto code (in reference to *Goto 2003* [11]) in the literature and will be denoted as G-CRM. The second code [38] makes use of cross-sections and computational routines available from the atomic data analysis structure (ADAS) database and will be denoted as A-CRM. Table 2 summarizes the data sources implemented by these codes. G-CRM uses EIE and ionization cross-sections from Ralchenko *et al* [41] for states $n \leq 4$, uses scaling laws for $5 \leq n \leq 20$ [9, 10], and assumes that states $21 \leq n \leq 26$ are described by a Saha–Boltzmann equilibrium. A-CRM implements EIE cross-sections from Ballance *et al* [42] but ionization cross-sections from Ralchenko *et al* [41]. For completeness, it is noted that G-CRM accounts for the mixing of singlet and triplet atomic states by a finite magnetic field and A-CRM does not account for a magnetic field. However, the effects of the magnetic field at TCv’s 1.4 T field are negligible.

The predicted line ratios of excitation-driven emission for $\frac{3^1S \rightarrow 2^1P}{3^1D \rightarrow 2^1P}$, i.e. $\text{Lrt}(\frac{728 \text{ nm}}{668 \text{ nm}})$, and $\frac{3^3S \rightarrow 2^3P}{3^1D \rightarrow 2^1P}$, i.e. $\text{Lrt}(\frac{728 \text{ nm}}{668 \text{ nm}})$, by G-CRM at $B = 1.4 T$ and by A-CRM are shown in figure 3. Direct comparisons of G-CRM at $B = 1.4 T$ to A-CRM and to G-CRM at $B = 0$ are shown in figure 4. As will be discussed in section 7, G-CRM was found to produced T_e and n_e measurements in good agreement with those of Thomson scattering, whereas A-CRM was found to systematically overestimate the temperature. The root of this overestimation by A-CRM is that A-CRM predicts $\text{Lrt}(\frac{728 \text{ nm}}{706 \text{ nm}})$ ’s that are $\sim 20\%$ smaller for a given T_e than what is observed and predicted by G-CRM. Due to this disparity in performance, only HeMSI measurements produced with G-CRM are presented in section 7 and are the focus of this work. Both codes are noted here as both are still

employed frequently in plasma research. For works employing and related to G-CRM, see [9–11, 18–21, 24, 27, 31–33, 37, 45–62] and for those employing, and related to A-CRM, see [13, 14, 38, 42, 63–68].

3. MANTIS spectral cameras

The MANTIS diagnostics are high-resolution multi-spectral cameras. Each MANTIS diagnostic implements a polychromator design that filters light through the repeated reflection of the light by band-pass filters, which have pass-bands of ~ 1.5 nm. Light which passes through a filter is imaged onto a CMOS detector. An original ten-channel diagnostic was described in Perek *et al* [6], and an additional six-channel system has since been installed. Both systems have toroidally tangential views of TCv. The six-channel system views the plasma from the mid-plane and the ten-channel system views the plasma from 0.450 m below the mid-plane. Figure 5 illustrates the installation of the MANTIS cameras on TCv and examples of images taken from both systems. In this work, the 16 camera detectors operated at 200 frames per second with 12 bits of dynamic range and the pixels were square in shape. The gain and exposure times were adjusted dynamically to avoid overexposure.

For HeMSI, two He I singlet lines, 728.2 nm ($3^1S \rightarrow 2^1P$) and 667.8 nm ($3^1D \rightarrow 2^1P$), two He I triplet lines, 706.5 nm ($3^3S \rightarrow 2^3P$) and 587.6 nm ($3^3D \rightarrow 2^3P$), and a He II line, 468 nm ($4 \rightarrow 3$), were observed. During the course of the experimental campaign, a single Phantom fast-camera [69], which can image the whole lower divertor at a 150 kHz framerate, was introduced in place of the standard camera to observe the 587 nm ($3^3D \rightarrow 2^3P$) transition. The Phantom camera’s sensitivity was not calibrated at the time of writing. Discharges conducted after the installation of the fast-camera only use the 668, 706, and 728 nm He I lines for the T_e and n_e fits.

3.1. System calibration

The absolute brightnesses of the images are calibrated using an integrating sphere coupled to a broadband lamp. The spectral radiance of the broadband light at the output of the integrating sphere, the transmission of the band-pass filters, and their respective uncertainties are assumed to be known from the data provided by their manufactures. The uncertainty in the radiance of the lamp was given as 3%. The filters’ transmission profiles were provided at 0.05–0.1 nm increments about their band-passes with each transmission having an uncertainty of

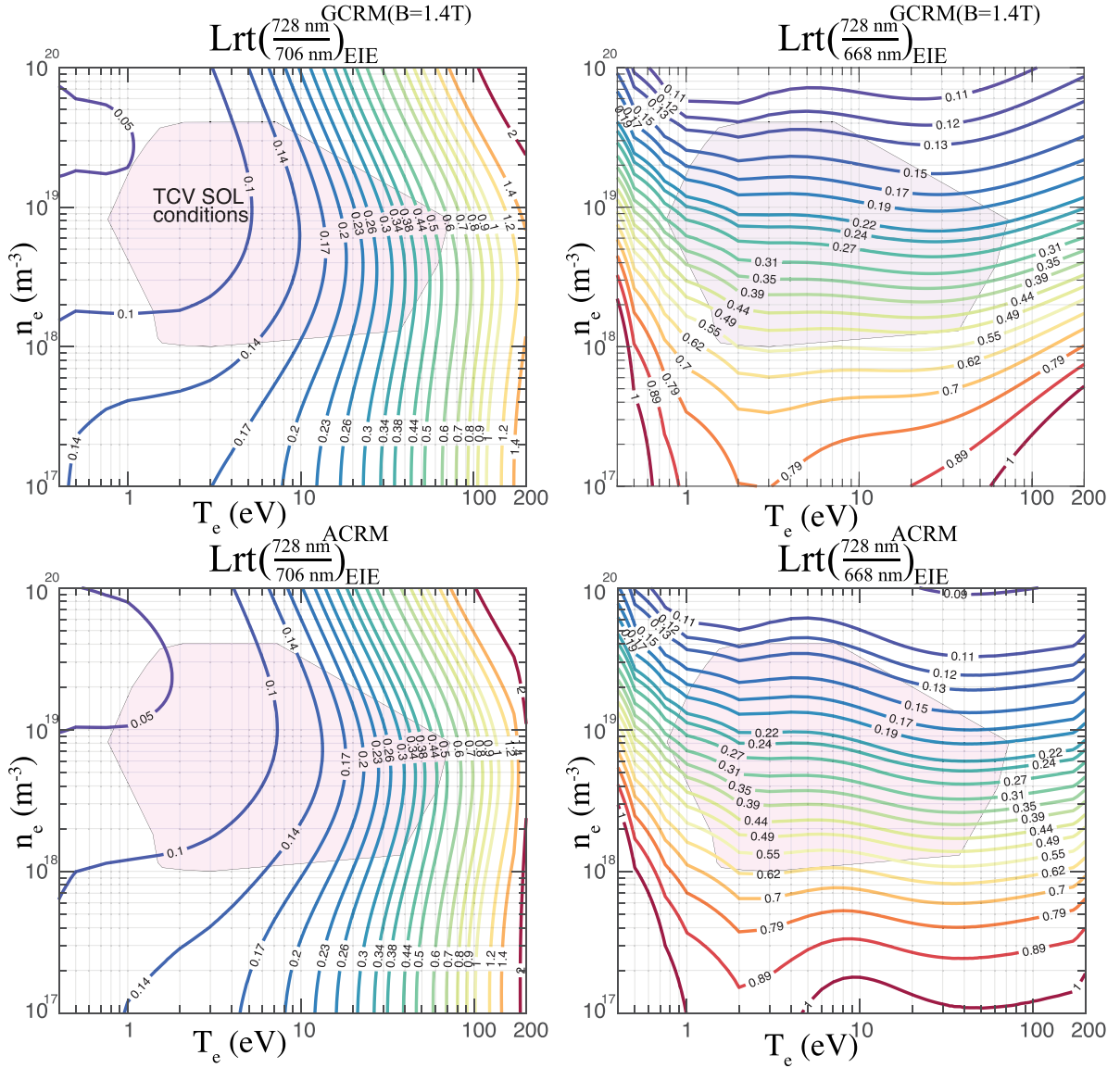


Figure 3. Contour plots of $Lrt(\frac{728\text{ nm}}{706\text{ nm}})$ and $Lrt(\frac{728\text{ nm}}{668\text{ nm}})$ for EIE driven emission for G-CRM at $B = 1.4T$ and A-CRM.

$< 1\%$. Note that these specifications detail how the filters perform within the optical layout of MANTIS, a converging beam of light with 2.3° half-cone angle about an average angle of incidence of 3° .

When observing a brightness source with MANTIS, the counts per second measured by a pixel, p_i , is related to the radiance of the source by:

$$p_i = \int_{\Omega} \int_A \int_{\nu} \alpha_i(\nu) B(\nu) f(\nu) d\nu da d\omega = \Omega_i A_i \int_{\nu} \alpha_i(\nu) B(\nu) f(\nu) d\nu \quad (13)$$

where A_i is the area of the sphere viewed by the pixel, Ω_i is the solid angle subtended by the aperture of the optics about the area being viewed, $\alpha_i(\nu)$ is an efficiency coefficient incorporating the quantum-efficiency of the detector and transmission of the optical system, $f(\nu)$ is the transmission of the band-pass filter, and $B(\nu)$ is the radiance of the source. $B(\nu)$ and $\alpha_i(\nu)$ are

assumed to be constant about the center-wavelength, ν_o , of the 1.2 nm wide band-pass of the filter. Therefore:

$$p_i = \alpha_i(\nu_o) B(\nu_o) \Omega_i A_i F \quad (14)$$

$$F \equiv \int_{\nu_o - \delta\nu}^{\nu_o + \delta\nu} f(\nu) d\nu. \quad (15)$$

The calibration factor γ_i for the pixel is then defined as:

$$\frac{1}{\gamma_i} \equiv \frac{p_i}{B(\nu_o) F} = \Omega_i A_i \alpha_i(\nu_o). \quad (16)$$

Now, instead of a broadband source, assume a monochromatic source of light, $L^m(\nu_o)$, is input into the system. The signal per second on the pixel, p_i^m , is then:

$$p_i^m = \alpha(\nu_o) \Omega_i A_i L^m(\nu_o) f(\nu_o). \quad (17)$$

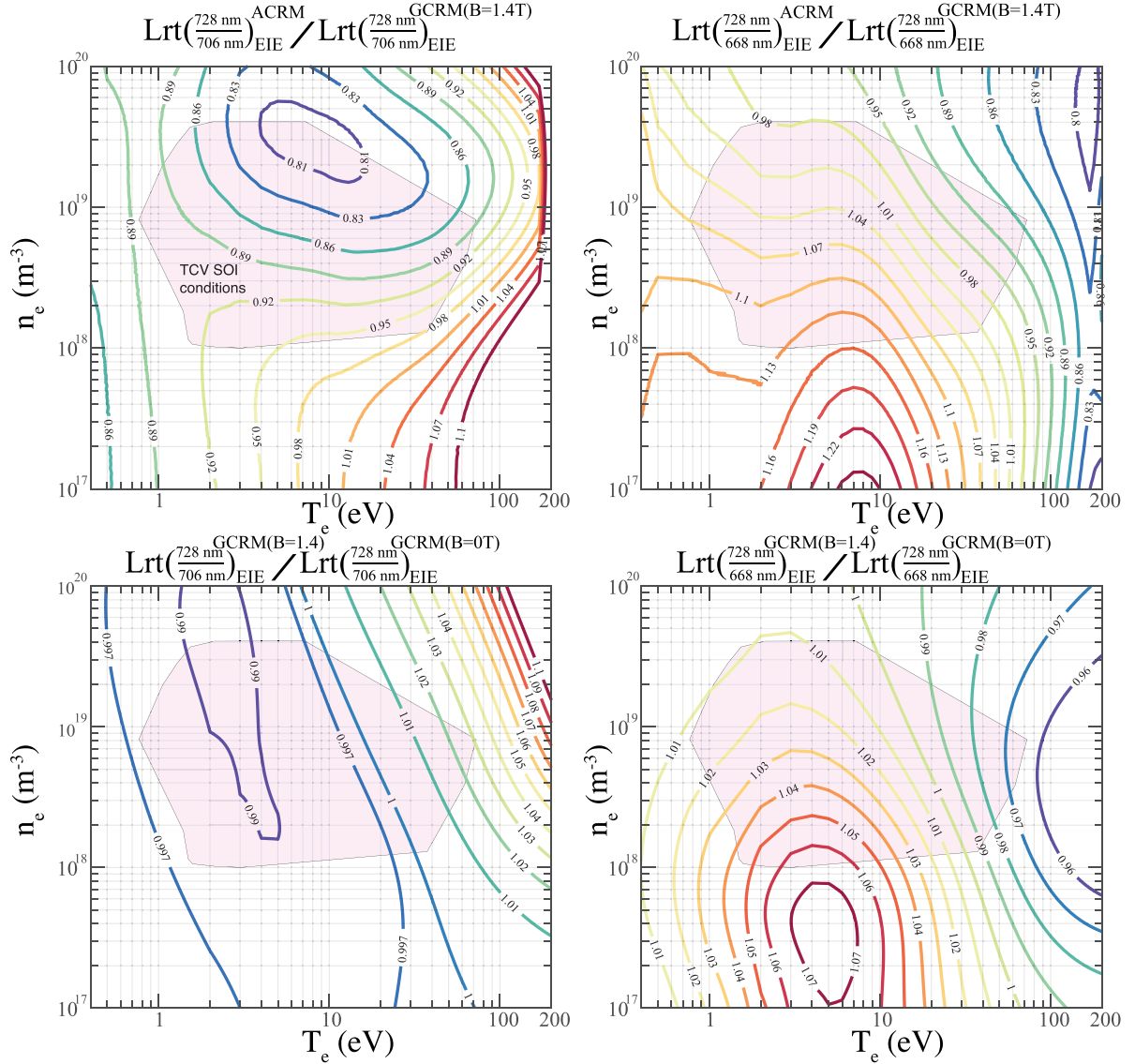


Figure 4. Ratio of predicted line-ratios from G-CRM at $B = 1.4$ to A-CRM and G-CRM at $B = 0$.

This permits the measurement of $L^m(\nu_o)$ via the calibration factor, γ_i , i.e.:

$$\frac{\gamma_i}{f(\nu_o)} p_i^m = L^m(\nu_o). \quad (18)$$

3.2. Inversion of the images

The emissivity of a plasma, $\epsilon(\vec{r})$, has dimensions of ($\frac{\text{photons}}{\text{s} \cdot \text{m}^3}$). The counts per second recorded by a pixel, p_i , is related to the emissivity, which is assumed constant in time, by:

$$\begin{aligned} p_i^m &= f(\nu_o) \alpha(\nu_o) \int_{\Omega} \int_T \int_A \int_l \epsilon(\vec{r}) / (4\pi) d\Omega dA dl \\ &= f(\nu_o) \alpha(\nu_o) \Omega_i A_i \int_L \epsilon(\vec{r}) dl \end{aligned} \quad (19)$$

where l is the length along the pixel's line-of-sight. In integrating over $d\omega$ and da it has been implicitly assumed that plasma emission is isotropic, and that the rays are pencil thin, i.e.

$\epsilon(\vec{r})$ is constant for a given value of l . Applying the system calibration:

$$\frac{\gamma_i}{f(\nu_o)} p_i^m = \int_L \epsilon(\vec{r}) dl. \quad (20)$$

When inverting the images, ϵ is assumed to be toroidally symmetric, i.e. $\epsilon(\vec{r}) = \epsilon(r, z)$. By discretizing in the poloidal plane, equation (20) becomes

$$b_i \equiv \frac{\gamma_i}{f(\nu_o)} p_i^m = \sum_j ds_{(i,j)} \epsilon_j \quad (21)$$

$$\rightarrow \vec{b} = K \cdot \vec{\epsilon} \quad (22)$$

where $K_{(i,j)} = ds_{(i,j)}$ is the geometric transfer matrix. This matrix represents the length of the i th ray subtending the j th voxel. For the tomographic inversions performed in this work, the images were down-sampled by a factor of 4 (factor of 2 along the detectors' rows and columns). The software Calcam was

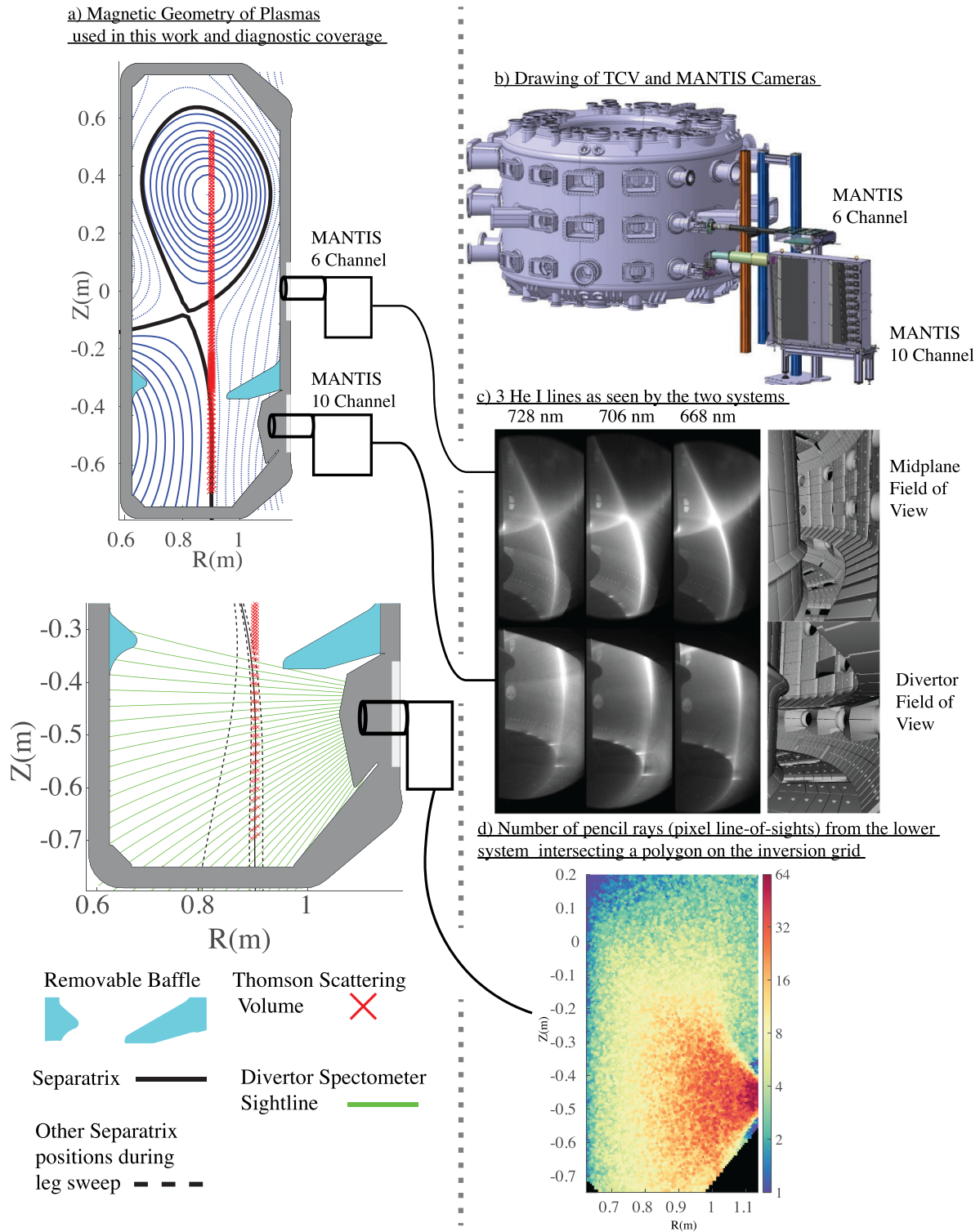


Figure 5. (a) Display of the poloidal cross-sections of the magnetic configuration used in the experiments and the TCV vessel. The top plot displays the whole vessel cross-section, while a magnification of the divertor region is shown below it. The dotted black lines in the magnified divertor drawing indicate the different positions through which the outer divertor leg was swept. The modification of the vessel's profile due to the baffle is shown in blue. Also indicated on the cross-section are the poloidal locations of the MANTIS cameras, Thomson scattering volumes, and spectrometer lines of sight. (b) Drawing of TCV and the MANTIS cameras. (c) Example images, which have been normalized, from three helium lines taken during the experiments, and a synthetic view produced from the calcam software [70]. (d) Number of pixels whose line of sight intersects a given triangle of the inversion grid.

used to register the cameras' positions and create the geometric transfer matrices [70]. The down-sampled images each contained approximately 10^5 pixels, whereas the inversion grid was constructed of 14 549 triangular cells. Therefore, the reconstruction problem was over-determined and no external regularization was required to reconstruct the emissivities. In figure 5(d), the number of down sampled pixels whose line of sight traverses a given polygon in the inversion grid is shown. As the $K_{(i,j)}$'s were large and non-sparse matrices, calculating the pseudo-inverse of the K 's for the purpose of inverting the images was unfeasible. Instead of using the pseudo-inverse, the SART algorithm [71] was used to iteratively solve for $\vec{\epsilon}$.

4. A qualitative description of the multi-spectral images and emissivities

In order to better contextualize the HeMSI measurements, a montage of He I, He II (468 nm), and C III (465 nm) images (all simultaneously imaged with MANTIS) and their inversions over the course of a density ramp are shown in figure 6. The C III line is displayed because it is a low-temperature indicator. It sharply transitions from emitting to non-emitting for TCV densities, $n_e \approx 1 \times 10^{19}$, at $T_e \lesssim 8$ eV [5, 72]. In section 7, it will be shown that HeMSI produces accurate measurements for ionizing plasma conditions. The C III line can be used to validate this criterion when HeMSI is applied independent of Thomson scattering in the future. Note that the plasma equilibrium in figure 6 differs from that used in the validation experiments (see figure 5), and was chosen for this qualitative description because it shows a larger portion of the plasma boundary.

During the start of the density ramp in figure 6, $0.7\text{ s} < t < 1.1\text{ s}$, all lines emit along the whole length of the divertor leg with emission concentrated along the separatrix and common flux region. As the density is increased, the helium emission in the common flux region progressively diminishes downstream. This change coincides with the retraction of the C III and He II emission fronts from the outer target towards the X-point implying T_e is falling downstream. While the emission of the He I lines in the common flux region recedes with falling T_e , He I begins to emit within the private flux region. From $t > 1.3\text{ s}$, a new He II emission front emerges from the target moving towards the X-point, while the emergent He I emission front in the private flux region travels cross-field towards the separatrix. The disappearance and reemergence of emission fronts suggest that different atomic processes are producing each front.

As will be shown in section 7, HeMSI gives good agreement with Thomson scattering measurements for the He I emission produced during $0.7\text{ s} < t < 1.1\text{ s}$ when the plasma can still be described as ionizing. However, when $T_e < 10$ eV in deuterium plasmas, as it is for $t > 1.3$, the helium CRM's predictions of the 728 nm to 706 nm line-ratio diverge from the observed line ratios. In section 7, it is shown that this emission at low T_e cannot be explained by EIE or EIR indicating the existence of competing processes outside the CRM. Note

that non-ionizing majority helium plasmas were not observed as the helium plasmas would disrupt before a sufficiently low T_e could be reached. If a scenario with significant EIR were reached, the 468 nm He II line would have been used to constrain the amount of He I emission driven by EIR.

5. Experimental setup

A series of L-mode plasmas with the same single-null magnetic geometry (see table 3) was performed to compare HeMSI measurements to divertor Thomson scattering measurements. See [73] for information on the divertor Thomson scattering system. In order to maximize the spatial cross-coverage of both diagnostics, the plasma geometry was shaped such that the outer divertor leg of the separatrix was nearly parallel to the Thomson scattering laser's path. During a discharge, the plasma was brought to a specified value of line-averaged density. While maintaining this specified density, the position of the outer target was moved between discrete points about the Thomson scattering laser's path. This sweep produced 2D profiles of Thomson scattering T_e and n_e measurements. The 2D HeMSI measurements were acquired during the entire shot. The cameras operated at 200 Hz with exposure times dynamically adjusting between 0.2 ms to 5.0 ms to prevent saturation. Divertor spectrometers which viewed the divertor leg were utilized for the purpose of cross-checking the MANTIS measurements [74]. The emissivity profiles measured by MANTIS were found to accurately predict the brightness observations of the divertor spectrometers. Furthermore, the divertor spectrometers confirmed that there was negligible spectral contamination within the MANTIS filters' spectral bands. A poloidal cross-section displaying the magnetic equilibrium and diagnostic coverage is shown in figure 5.

Discharges were conducted for majority deuterium and majority helium plasmas. In deuterium plasmas at TCV, there is sufficient He emission for HeMSI due to the use of a helium glow between shots to clean the vessel. Nevertheless, for the validation experiments, additional helium was seeded during the ramp to the target density to increase the signal strength. Observing plasmas of both species was important for investigating the importance of different atomic mechanisms. Several works have reported photon-excitation, which is not accounted for in this work, as a factor in observed discrepancies between measurements and He CRMs' predictions [13, 18, 33, 50–52, 54, 75]. A majority helium plasma should exacerbate this effect if it is significant in the TCV divertor. It was found that HeMSI gave similar results for ionizing deuterium and helium plasmas supporting the decision to neglect photon-excitation.

Benchmarking discharges were performed for both toroidal field directions. The two field-directions engender distinct n_e and T_e profile shapes about the separatrix [76, 77]. Observing plasmas in both field-directions tested whether HeMSI could resolve the changes in profiles. In this work, '*forward-field*' refers to a discharge in which B_t is directed clockwise when looking from above (∇ -B drift favorable to H-mode), and

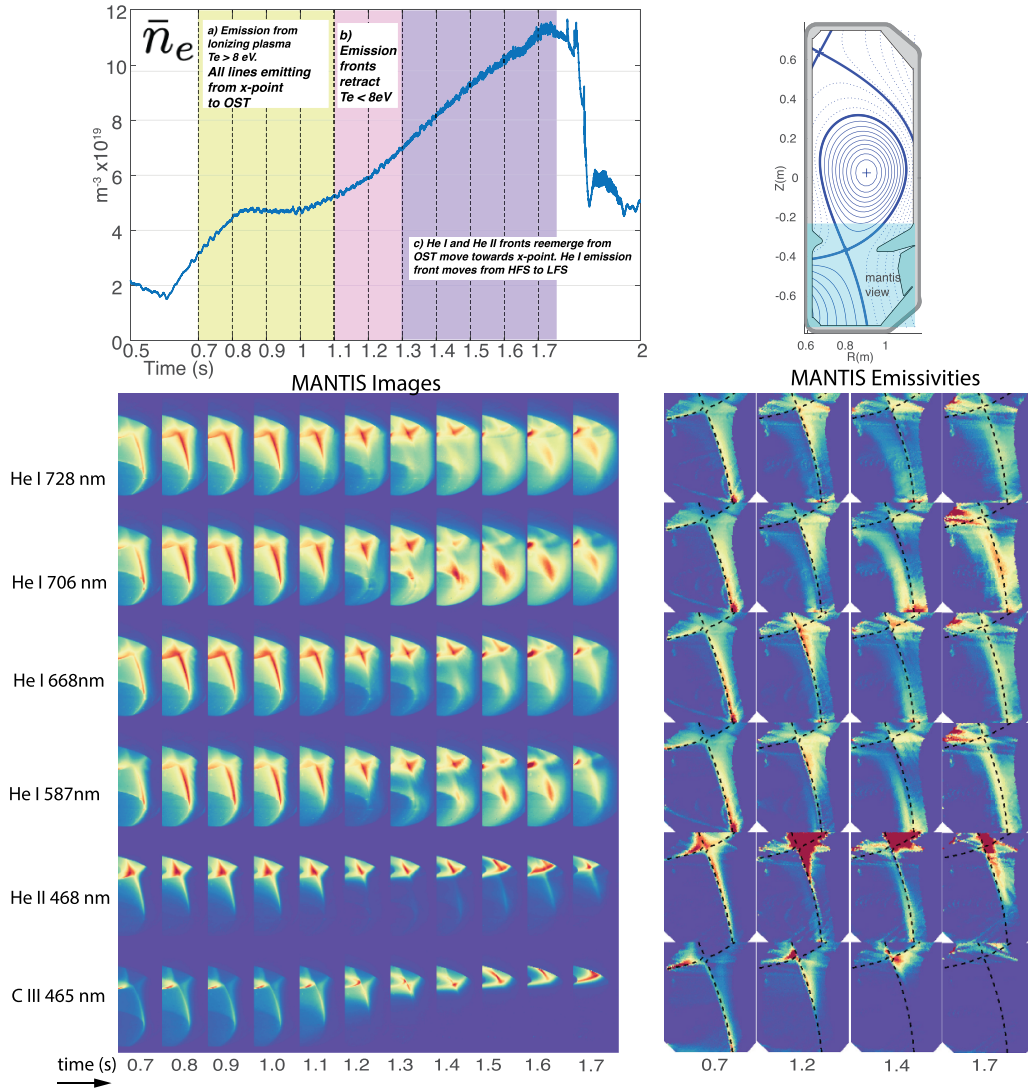


Figure 6. Montage of He I, He II, and C III images and emissivities during a density ramp of deuterium plasma. The color scale for each individual image and inversion is arbitrary. See section 4.

‘reversed-field’ refers to a discharge in which B_r is directed counter-clockwise ($\nabla \cdot B$ drift unfavorable to H-mode).

During the experimental campaign, divertor baffles were installed and removed periodically [3, 78, 79]. The change to the vessel’s poloidal cross-section due to the ‘long’ low-field-side baffles is shown in figure 5. The presence of baffles increased the neutral compression within the divertor [3, 78, 79]. A gas injection system was also installed into the low-field-side baffle, and used to produce a localized gas puff of helium into deuterium plasmas. Localized gas puffs allowed the application of the HeMSI technique under conditions in which the need for an inversion was removed. The results from this methodology are reviewed in section 7.3. As expected, the puff and inversion methodologies produced similar agreement with Thomson scattering. A difference in the results of the two methodologies would have implied an error in the application of HeMSI. Thus, the results from both methodologies are shown to demonstrate that the two applications are consistent with each other.

6. Comparison methodology

To facilitate the comparison between the T_e and n_e measurements from HeMSI and Thomson scattering, all measurements were parsed into a discrete (ρ, Z) bin with ρ defined as:

$$\rho(\psi) = \sqrt{1 - \frac{\psi}{\psi_o}} \quad (23)$$

where ψ denotes the poloidal magnetic flux such that $\psi = 0$ at the separatrix and ψ_o is the flux at the magnetic axis. Both sets of measurements were spatially and temporally averaged within these (ρ, Z) bins. Each co-temporal set of HeMSI images generates a set of T_e and n_e measurements spanning the whole (ρ, Z) space of interest. However, successive Thomson scattering measurements were required to discern T_e and n_e profiles for comparison with the inherently 2D HeMSI results. Therefore, only the time-averaged Thomson scattering and HeMSI measurements were compared. The data were

averaged over time intervals in which \bar{n}_e was held constant. The temporal variations within the HeMSI measurements were driven primarily by sawtooth oscillations in the core plasma. This variation was negligible compared to the spatial gradients of T_e and n_e . The binned profiles were used to compare the two measurements. In order to present these comparisons, the HeMSI and Thomson scattering measurements are presented together in 1-D plots versus a ρ axis. In these plots, the error bars assigned to the HeMSI measurements correspond to the average absolute deviation within each (ρ, Z) bin such that the width of the error bar is two standard deviations of the average value.

Examples of HeMSI profiles compared to Thomson profiles are shown in the bottom two panels of figure 7. The steps of averaging the data for the comparison are illustrated in figure 8. The top two plots in figure 7 display the time-averaged 2D HeMSI measurements. In section 7, the results from other discharges will be presented in the same format as figure 7.

6.1. Sources of uncertainty

As noted in section 6, the error bars assigned to the HeMSI measurements represent the variance, precision, of the measurements. This assignment neglects the uncertainties associated with the relative calibration of the images, inversion of the images, and the atomic data used in the CRM. These uncertainties, which were taken to be either negligible or unfeasible to quantify, are discussed here. Note that this work is motivated to a large degree by complex uncertainties such as those associated with toroidal asymmetries and the atomic data. The comparisons of HeMSI with Thomson scattering gauge whether these uncertainties are of a magnitude to inhibit HeMSI. The striking agreement observed between HeMSI and Thomson scattering in many scenarios suggests that these uncertainties are encompassed within the scatter of the data. However, cases of systematic disagreement between Thomson scattering and HeMSI do exist, so the neglected uncertainties will be revisited in section 7.

6.1.1. Uncertainty of brightness measurements. As stated in section 3.1, the source used to calibrate the MANTIS cameras has an uncertainty of approximately 3% associated with its absolute magnitude. Therefore, the relative brightness measurements have an uncertainty of less than 3%. The scatter in the relative brightness measurements dominates this uncertainty. Thus, the uncertainty associated with the relative calibration is negligible.

6.1.2. Uncertainties of image inversion. The uncertainty of the inversion process arises from three components: the camera's spatial registration, the resolution of the camera and inversion grid, and the validity of toroidal symmetry.

A spatial calibration was performed for each camera on every discharge. After the registration, the images were downsampled by a factor of 4 before being inverted. Downsampling the images diminishes any misalignment that remained after

the manual registration at full resolution. The registrations were observed to be highly accurate, so the uncertainty of the registration is taken to be negligible.

The downsampled images contained approximately 10^5 square pixels and the triangular inversion grid had 14 549 cells with a median side length of 8.5 mm. The resolution of the camera is considered sufficient, but the analysis could benefit from a finer inversion grid. However, this analysis was performed in MATLAB on a single CPU, so extending the grid was computationally prohibitive at the time of writing. Consequently, the size of the inversion grid cell may obscure the sharp falloff in emission when going from the separatrix to the private flux.

The assumption of toroidal symmetry is necessary for this analysis, and violation of this axiom within the cameras' views will produce artifacts in the inversions. Quantifying the effects of toroidal asymmetries on the HeMSI measurements is a non-trivial task. The possibility of toroidal asymmetries arising in the bulk plasma are acknowledged, but estimating their magnitude is beyond the scope of this work.

The surface of the vessel is toroidally asymmetric. Thus, light emitting from the surface of the vessel produces toroidally asymmetric features in the images. The ability to resolve these features in the image makes their discussion tractable. Emission from the surface can be caused by reflected light, or plasma surface interactions such as at the target. The significance of reflections was estimated by observing the signals of pixels whose lines of sight only traverse the far common flux region. The signals of these pixels were assumed to be dominated by reflected light.

To mitigate the effects of reflections the HeMSI analysis was constrained to a narrow region about the separatrix of the outer-leg, $0.98 \leq \rho \leq 1.05$. This region spans from 1 cm into the private flux region to 3 cm into the common flux region. For ionizing plasmas, the effects of reflections will be negligible in this region since the plasma's emission dominates. For the case of a non-ionizing plasma, reflections are non-negligible. However, in such cases, the flux aligned emission structures along the leg appear to still be sufficiently resolved. An explanation of this could be that the vessel's illumination is sufficiently symmetric about the torus such that the inversion is able to disentangle the emission of the plasma from reflections at the wall. Examples of inversions of non-ionizing plasmas can be viewed in figure 6 for $t \geq 1.4$.

The surface of the strike point is toroidally asymmetric, so plasma surface interactions at the strike-point produce artifacts in the inversion. However, in this work, Thomson scattering measurements were compared to HeMSI measurements at locations which were at least 5 cm away from the vessel. Thus, the artifacts produced via emission from plasma surface interactions at the target have a negligible effect on the region of comparison.

Relevant to this discussion is Carr *et al* [80] which reported on the effects of reflections on spectral image inversions in tokamaks. In this work, the CHERAB software [81] was used to perform inversions of spectral images from JET with and without accounting for reflections. It was found that a significant amount of reflected light originates from the strike-point,

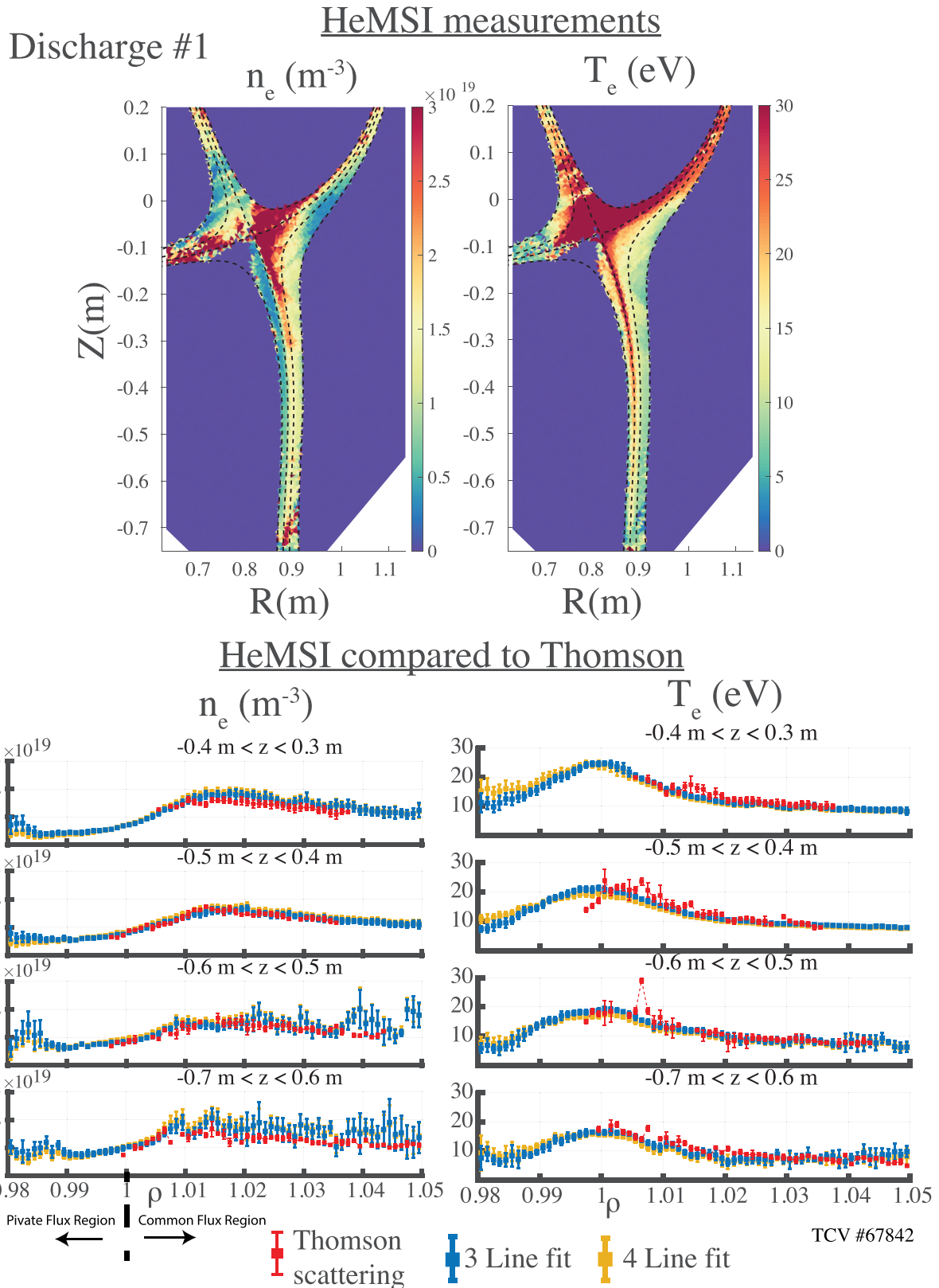


Figure 7. Discharge #1. Reversed-field helium plasma with $\bar{n}_e = 8 \times 10^{19} m^{-3}$ and an unbaffled divertor. HeMSI evaluations are shown with and without inclusion of 587 nm line.

and this light can have a strong effect on the region immediately surrounding the target. However, the effects of reflections were negligible in the rest of the poloidal plane (see figure 12

in [80]). Furthermore, Carr 2019 reports on analysis performed on JET, a metal wall tokamak, and notes that reflections will have a smaller effect on a carbon wall tokamak like TCV. In

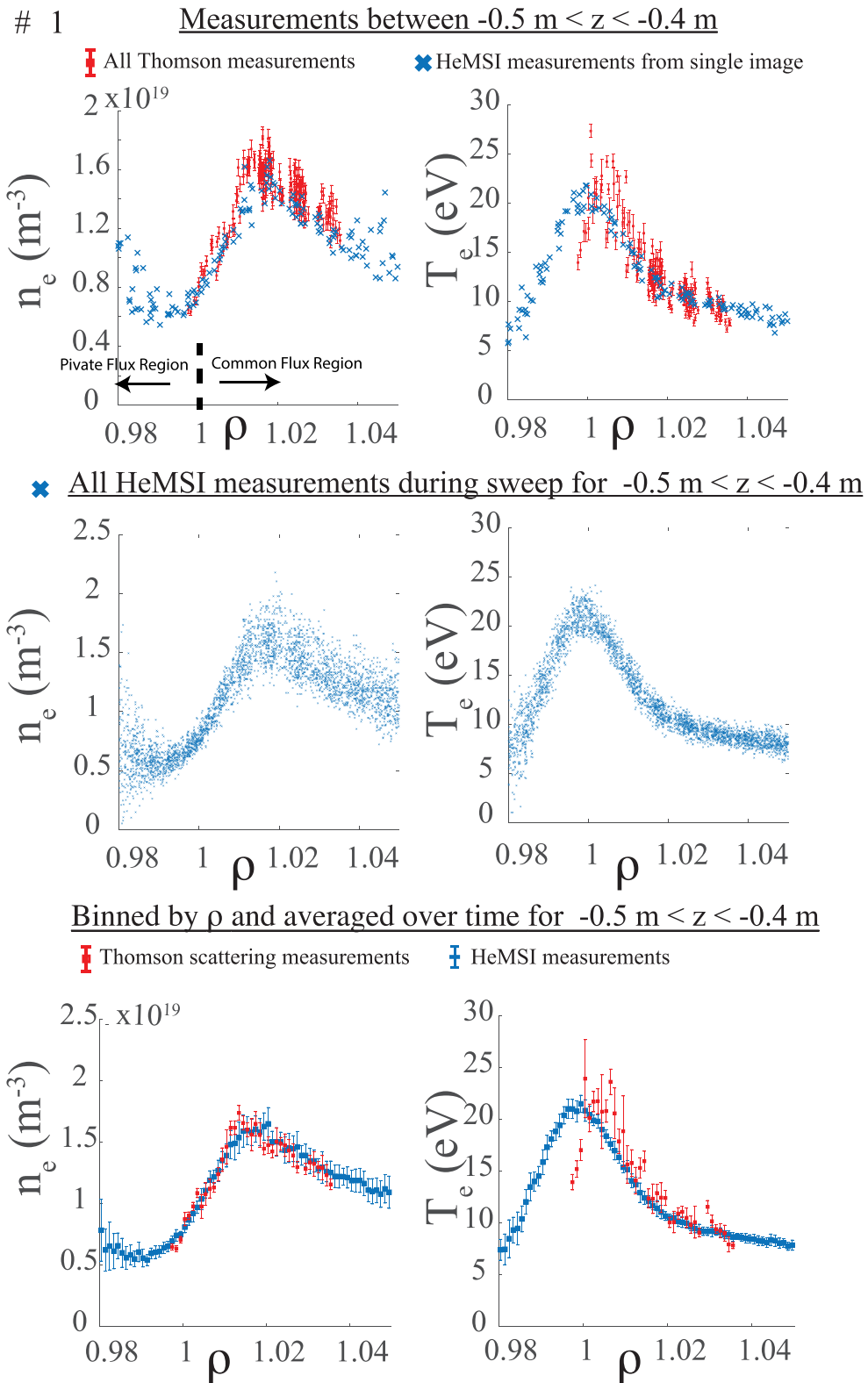


Figure 8. Depiction of data shown in figure 7 before and after averaging. The top row displays HeMSI measurements from a single image between $-0.5 \leq z \leq -0.4$ in blue. The Thomson scattering measurements acquired during the entire leg sweep in this spatial range are shown in red. The second row shows each HeMSI measurement within $-0.5 \leq z \leq -0.4$ that was collected during the leg sweep. The last row shows both measurements binned onto a single ρ axis with bin sizes of $\delta\rho = .001$. The error bars were estimated from the standard-deviation within each bin.

future works, reflections can be incorporated into the HeMSI analysis like they are in Carr 2019 to remove artifacts and better resolve areas of weaker emission.

6.1.3. Uncertainty of CRM. Uncertainties in the atomic data are not provided in the CRM codes discussed in this work, G-CRM or A-CRM. Therefore the effects of uncertainties in the atomic data are not quantified. Nonetheless, uncertainties in atomic rates can produce large uncertainties in the inferred T_e and n_e [68]. This conclusion is evident in the differences between line-ratio predictions from G-CRM and A-CRM (see section 2.2 and figure 4). A benefit of this work is that it provides a direct test of these CRM codes with He I measurements that have been decoupled from line-integral effects and independent T_e and n_e measurements from Thomson scattering.

7. Results and discussion

The principal conclusions of this work are as follows. First, when employing G-CRM, HeMSI demonstrated consistently good agreement with Thomson scattering at the separatrix and in the common flux region, but intermittent agreement in the private flux region for:

- majority helium plasmas
 - * $5\text{ eV} \leq T_e \leq 60\text{ eV}$
 - * $2 \times 10^{18}\text{ m}^{-3} \leq n_e \leq 3 \times 10^{19}\text{ m}^{-3}$
- majority deuterium plasmas
 - * $10\text{ eV} \leq T_e \leq 40\text{ eV}$
 - * $2 \times 10^{18}\text{ m}^{-3} \leq n_e \leq 3 \times 10^{19}\text{ m}^{-3}$.

For deuterium plasmas with $T_e < 10\text{ eV}$, HeMSI overestimated T_e with respect to Thomson scattering. This overestimation was due to the measurements of $\text{Lrt}(\frac{728\text{ nm}}{706\text{ nm}})$ which were 2 to 3 times larger than would be expected for $T_e < 10\text{ eV}$. However, in this colder regime, the HeMSI measurements of n_e remained in good agreement with those of Thomson scattering. Disagreements in the private flux region were characterized primarily by an overestimation of n_e by HeMSI. This overestimation was driven by measurements of $\text{Lrt}(\frac{728\text{ nm}}{668\text{ nm}})$ being 2 to 3 times lower than expected.

To elaborate on these results, HeMSI and Thomson scattering measurements from six individual discharges are presented (see table 3). The discussion of these discharges follows in sections 7.1.1–7.1.6 with each emphasizing a salient feature of the HeMSI measurements. After presenting these individual discharges, the HeMSI measurements will be shown in aggregate as functions of T_e and n_e Thomson scattering measurements. This method reveals how the accuracy of HeMSI changes with local plasma conditions. Lastly, the HeMSI measurements from a localized gas puff into a majority deuterium plasma are demonstrated to be consistent with the measurements produced by inverting entire images.

7.1. Individual HeMSI poloidal maps compared to Thomson scattering

Two types of figures will be referenced in the following discussion of individual discharges. The first, which was described in section 6, directly compares 2D profiles of T_e and n_e from HeMSI and Thomson scattering. The second compares observed line ratio profiles $\text{Lrt}(\frac{728\text{ nm}}{706\text{ nm}})$ and $\text{Lrt}(\frac{728\text{ nm}}{668\text{ nm}})$ against synthetic profiles constructed by forward modeling the Thomson scattering measurements with G-CRM. This comparison is shown for $-0.5\text{ m} \leq z \leq -0.4\text{ m}$ for five discharges in figure 16.

7.1.1. HeMSI accurately reproduces Thomson scattering measurements for both deuterium and helium ionizing plasmas. Discharges #1 and #2 were majority helium and majority deuterium discharges, respectively. Although the species differed, both discharges were performed in the reversed-field configuration, without baffles, and had similar T_e and n_e profiles. In figures 7 and 9, the HeMSI measurements from both discharges are seen to be in excellent agreement with the Thomson scattering measurements. In discharge #2, Thomson scattering and HeMSI agree in both the common and private flux regions over the ranges of $10\text{ eV} \leq T_e \leq 40\text{ eV}$ and $2 \times 10^{18}\text{ m}^{-3} \leq n_e \leq 5 \times 10^{18}\text{ m}^{-3}$. Similar agreement is also observed in #1 over the ranges of $10\text{ eV} \leq T_e \leq 20\text{ eV}$ and $1 \times 10^{19}\text{ m}^{-3} \leq n_e \leq 1.5 \times 10^{19}\text{ m}^{-3}$. However, in #1, the Thomson scattering measurements were only collected in the common flux region.

Figure 16's first two rows contain the measured and synthetic $\text{Lrt}(\frac{728\text{ nm}}{706\text{ nm}})$ and $\text{Lrt}(\frac{728\text{ nm}}{668\text{ nm}})$ profiles from discharges #1 and #2. As would be expected from the similar T_e and n_e measurements, the two sets of observed ratios are similar to each other across the two discharges and both sets are in agreement with their synthetic counterparts. This gives confidence that the CRM correctly describes helium emission in the boundary of an ionizing plasma.

7.1.2. HeMSI's sensitivity to T_e . The sensitivity of HeMSI to changes in T_e will be highlighted here. During discharge #3, X2 electron cyclotron heating (ECH) was applied to the plasma at three different levels of input power, 1800 kW, 1200 kW, and 600 kW. Accounting for the Ohmic heating, the resultant total heating powers were 1890 kW, 1290 kW, and 820 kW, respectively. This is the only discharge discussed here that utilized auxiliary heating. For reference, the shots without auxiliary heating featured approximately 300 kW of Ohmic heating power. The HeMSI and Thomson measurements for the three levels of ECH input power are shown in figures 10 (1800 kW), 11 (1200 kW), and 12 (600 kW).

The discreet modulation of the X2 input power gives a clear demonstration of HeMSI's T_e sensitivity because the HeMSI and Thomson scattering measurements move in unison with the changing heating power. For example, the peak temperature drops for both measurements from $\sim 60\text{ eV}$ to $\sim 40\text{ eV}$ when the X2 power is decreased from 1800 kW to

Table 3. Description of the discharges that are individually presented in this paper. *rf* denotes that B_T is in the reversed-field direction (unfavorable to H-mode access), and *ff* denotes that B_T is in the forward-field direction (favorable to H-mode access).

Ref #	Fuel	$\bar{n}_e(10^{19} \text{ m}^{-3})$	w 587 nm	B_T Direction	Divertor Type	Figure
#1	Helium	8	Yes	<i>rf</i>	Unbaffled	7
#2	Deuterium	2	No	<i>rf</i>	Unbaffled	9
#3	Helium	2.5 (with X2 heating)	Yes	<i>rf</i>	Unbaffled	10–12
#4	Helium	7	No	<i>ff</i>	Unbaffled	13
#5	Deuterium	3	Yes	<i>rf</i>	Baffled	14
#6	Deuterium	6.5	No	<i>ff</i>	Unbaffled	15

1200 kW. Furthermore, the T_e profile is much broader for the 1800 kW and 1200 kW levels of input power than it is for the 600 kW level and the other Ohmic discharges. The $-0.6 \leq z \leq -0.5$ region in figure 11 (1200 kW) clearly illustrates this broadening. In all, the HeMSI measurements accurately resolve the T_e profiles about the separatrix for ionizing plasmas.

7.1.3. HeMSI resolves the effects of changing the B_T direction on the T_e and n_e profiles. In the section above, HeMSI was shown to capture the changes in the T_e profile caused by application of X2 heating. In this subsection, HeMSI is shown to resolve changes to the n_e and T_e profiles resulting from different B_T directions. The reversed-field direction of B_T produces a distinct n_e and T_e profile shape from the forward-field direction for sufficiently low temperature [76, 77]. Forward-field discharges have n_e profiles that peak at the separatrix, $\rho = 1.0$, and their T_e profiles fall off in a nearly linear manner going from the separatrix into the common flux region. For sufficiently low temperature, reversed-field discharges have n_e peaks well into the common flux region at $\rho > 1.01$, and their T_e profiles are concave. The two Ohmic reversed-field shots previously described, #1, and #2 (figures 7 and 9), exemplify these reversed-field characteristics. Discharge #4 was performed in forward-field. As shown in figure 13, HeMSI resolves the translation of the n_e profile while remaining in excellent agreement with the Thomson scattering measurements in the common flux region. The change in the T_e profile is also resolved by HeMSI, and HeMSI matches the T_e measurement from Thomson scattering in the private and common flux regions.

Comparing the $\text{Lrt}(\frac{728 \text{ nm}}{706 \text{ nm}})$ and $\text{Lrt}(\frac{728 \text{ nm}}{668 \text{ nm}})$ profiles for both field directions in figure 16 reveals stark differences. In the forward-field case (row 3 and discharge #4), $\text{Lrt}(\frac{728 \text{ nm}}{668 \text{ nm}})$ linearly increases from the separatrix into the common flux region while $\text{Lrt}(\frac{728 \text{ nm}}{706 \text{ nm}})$ decreases linearly in the common flux region. In the reversed-field cases (all other rows), $\text{Lrt}(\frac{728 \text{ nm}}{668 \text{ nm}})$ has a local minimum in the common flux and a concave $\text{Lrt}(\frac{728 \text{ nm}}{706 \text{ nm}})$ profile going from the separatrix into the common flux region. These subtle but resolved changes in the emission profiles and in the T_e and n_e profiles establish confidence in the inversion methodology and spatial resolution of HeMSI. The disagreements observed for the n_e and $\text{Lrt}(\frac{728 \text{ nm}}{668 \text{ nm}})$ profiles in the private flux region are discussed in section 7.1.5.

7.1.4. HeMSI measurements with baffled divertor. The presence of a divertor baffle increases the neutral density within the divertor volume [78]. Nonetheless, HeMSI and Thomson scattering measurements compared similarly for baffled and unbaffled conditions. The measurements from discharge #5, a baffled discharge, are an example of this result. As depicted in figure 14, HeMSI and Thomson scattering maintain good agreement in the common flux region and inconsistent agreement in the private flux region in this baffled discharge. This is consistent with the non-baffled results.

7.1.5. Disagreement between n_e measurements in the private flux region. Inconsistent agreement was observed between HeMSI and Thomson scattering measurements of n_e in the private flux region. The disagreement was observed in all ionizing forward-field shots but not all ionizing reversed-field discharges. For example, forward-field discharge #4 (figure 13) and reversed-field discharge #5 (figure 14) exhibited this disagreement. Like all ionizing forward-field discharges, the disagreement was seen throughout the whole private flux region in discharge #4; in the reversed-field case, #5, the disagreement is present in the private flux region for $z < -0.4$ m. On the other hand, discharge #2 (figure 9) manifests good agreement throughout the private flux for both T_e and n_e measurements.

The line-ratio profiles of discharges #4 and #5 are shown in rows 3 and 4 of figure 16, respectively. Therein, the measurements of $\text{Lrt}(\frac{728 \text{ nm}}{668 \text{ nm}})$ are seen to be the source of the disagreement. For both discharges, the synthetic $\text{Lrt}(\frac{728 \text{ nm}}{668 \text{ nm}})$ profiles increase as they cross the separatrix going into the private flux region. However, the observed $\text{Lrt}(\frac{728 \text{ nm}}{668 \text{ nm}})$ profile in the forward-field discharge is decreasing at this junction while that of the reversed-field discharge is flat. Note that the synthetic and observed $\text{Lrt}(\frac{728 \text{ nm}}{706 \text{ nm}})$ profiles in both discharges are in fair agreement.

The source of the intermittent n_e agreement in the reversed-field cases and complete lack of agreement in the forward-field cases for the private flux region is not currently understood. Thus, the discussion returns to the neglected uncertainties catalogued in section 6.1. The good agreement between the measured and synthetic $\text{Lrt}(\frac{728 \text{ nm}}{706 \text{ nm}})$ profiles in the private flux region suggests that the error originates with the 668 nm images. Reflections have been observed to be most prominent in images of the 728 nm line. Consequently, reflections are unlikely to be the root of this disagreement which appears

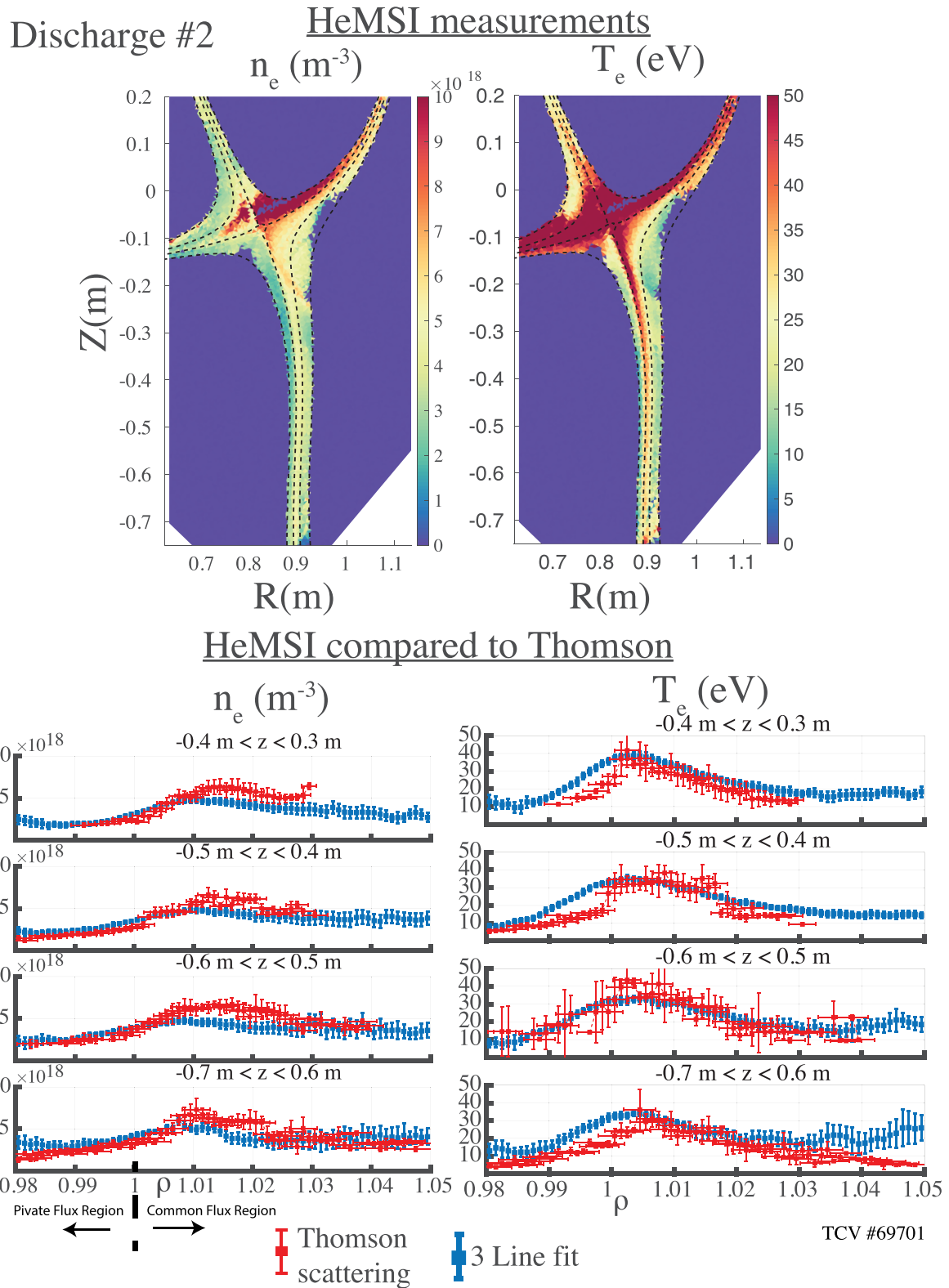


Figure 9. Discharge #2. Reversed-field deuterium plasma with $\bar{n}_e = 2 \times 10^{19} \text{ m}^{-3}$ and an unbaffled divertor. HeMSI evaluations did not include the 587 nm line.

to stem from the 668 nm line. Poor spatial registrations of the 668 nm camera can also be ruled out because registration errors would not discriminate between ionizing forward-field plasmas and reversed-field plasmas. The resolution of the

inversion grid is also not suspected as the T_e and n_e profiles are not notably sharper in these instances.

The observation that the discrepancy in the $Lrt(\frac{728 \text{ nm}}{668 \text{ nm}})$ ratio disappears in non-ionizing deuterium plasmas suggests that

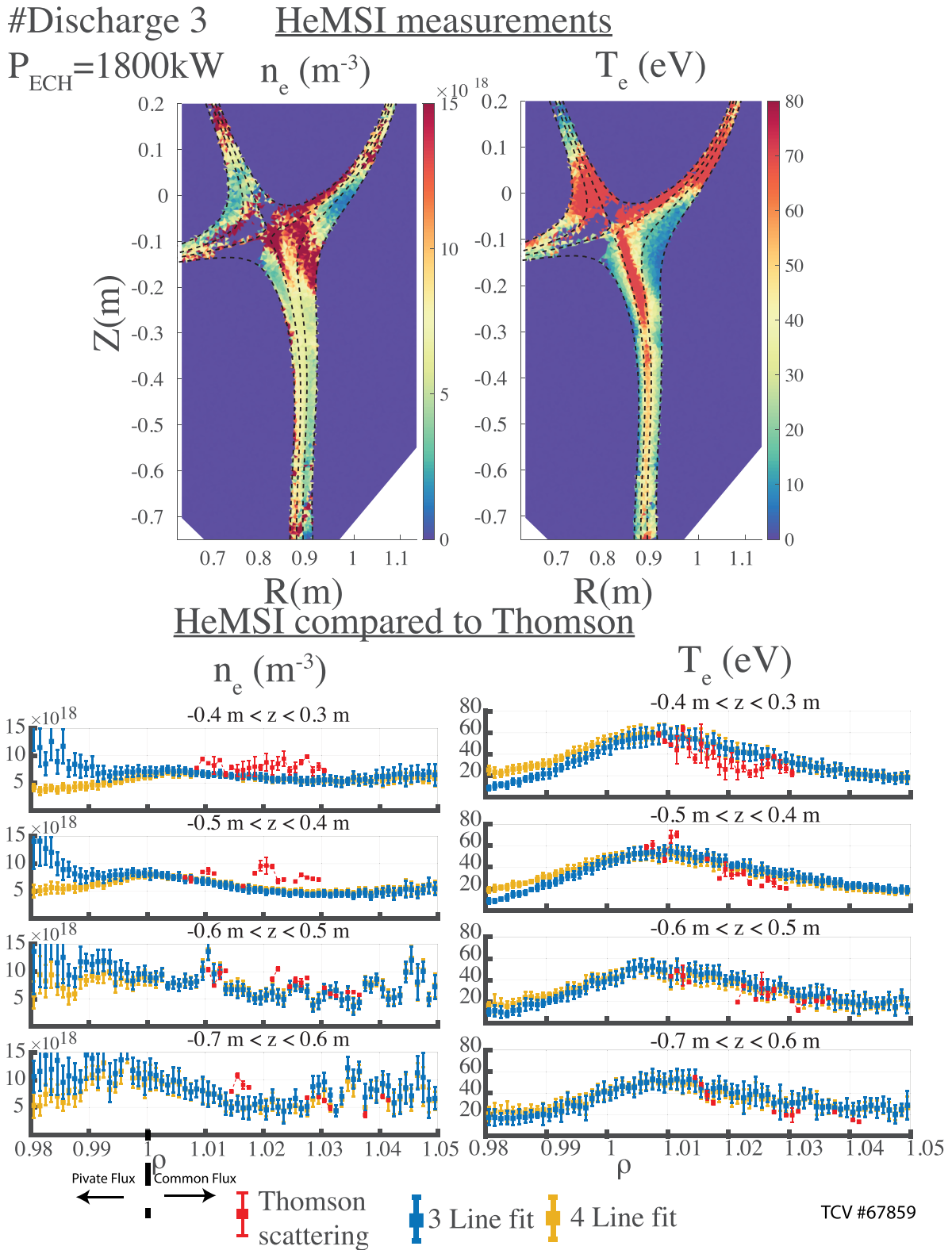


Figure 10. Discharge #3. Reversed-field helium plasma with $\bar{n}_e = 2.5 \times 10^{19} \text{ m}^{-3}$ with 1800 kW of X2. HeMSI evaluations are shown with and without inclusion of 587 nm line.

the cause lies in the modeling of the plasma and/or atomic physics. However, errors in the atomic rates are not suspected. The general good agreement in the common flux region precludes the discrepancy from being solely T_e and n_e dependent.

However, atomic or chemical processes beyond the CRM cannot be disregarded. Furthermore, the behavior could be due to toroidal asymmetries in the plasma volume. Such discrepancies could selectively affect the $Lrt(\frac{728 \text{ nm}}{668 \text{ nm}})$ ratio. Filaments

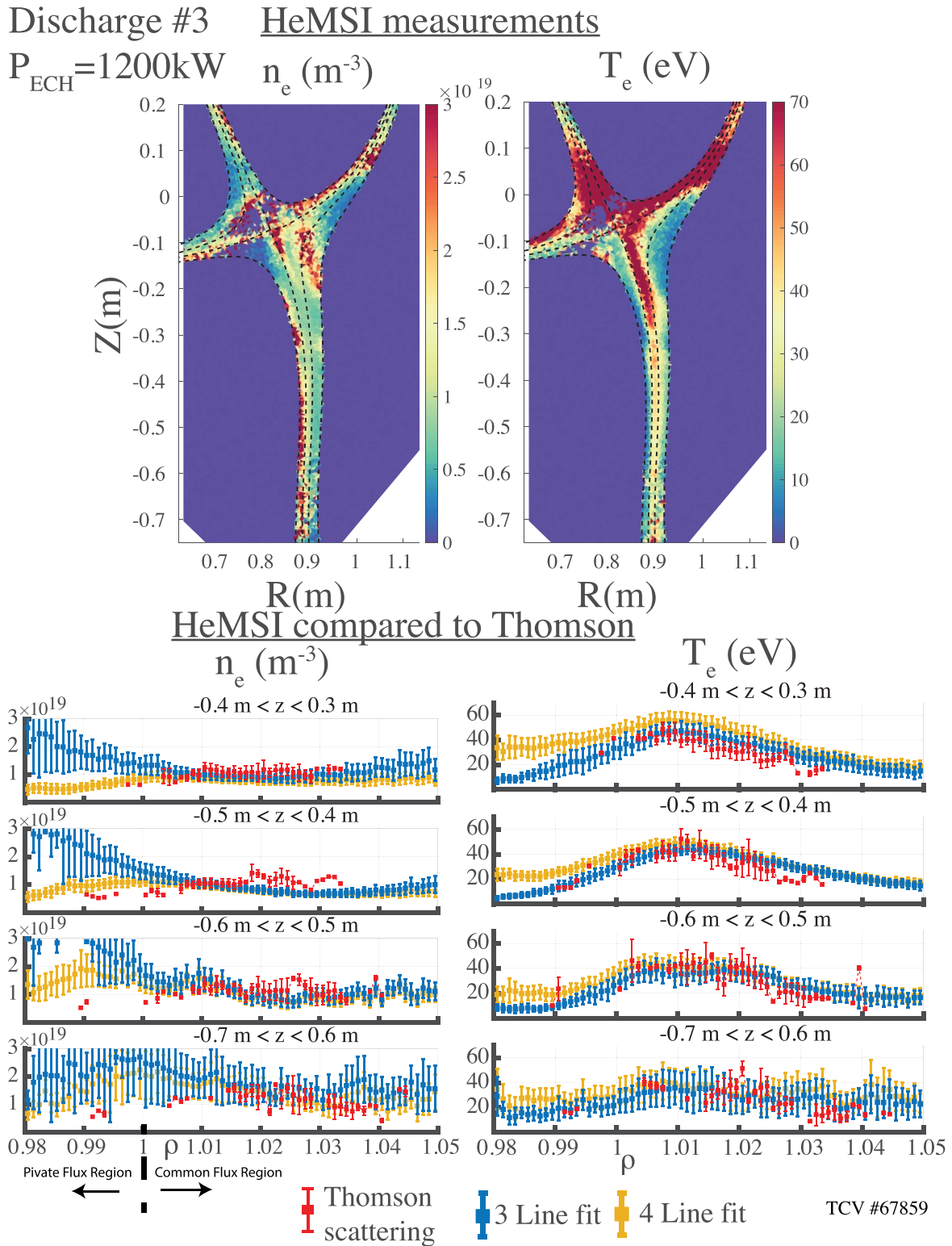


Figure 11. Discharge #3. Reversed-field helium plasma with $\bar{n}_e = 2.5 \times 10^{19} \text{ m}^{-3}$ with 1200 kW of X2. HeMSI evaluations are shown with and without inclusion of 587 nm line.

could also be the root of the disagreement. Filaments could cause the brightness of He I lines to significantly differ during the exposure time of the images and/or produce toroidal asymmetries [62].

Opacity is not suspected to play a role. The disagreement is observed in ionizing forward-field deuterium plasmas. If opacity were important in these deuterium cases, it would be even more important in all instances of helium plasmas.

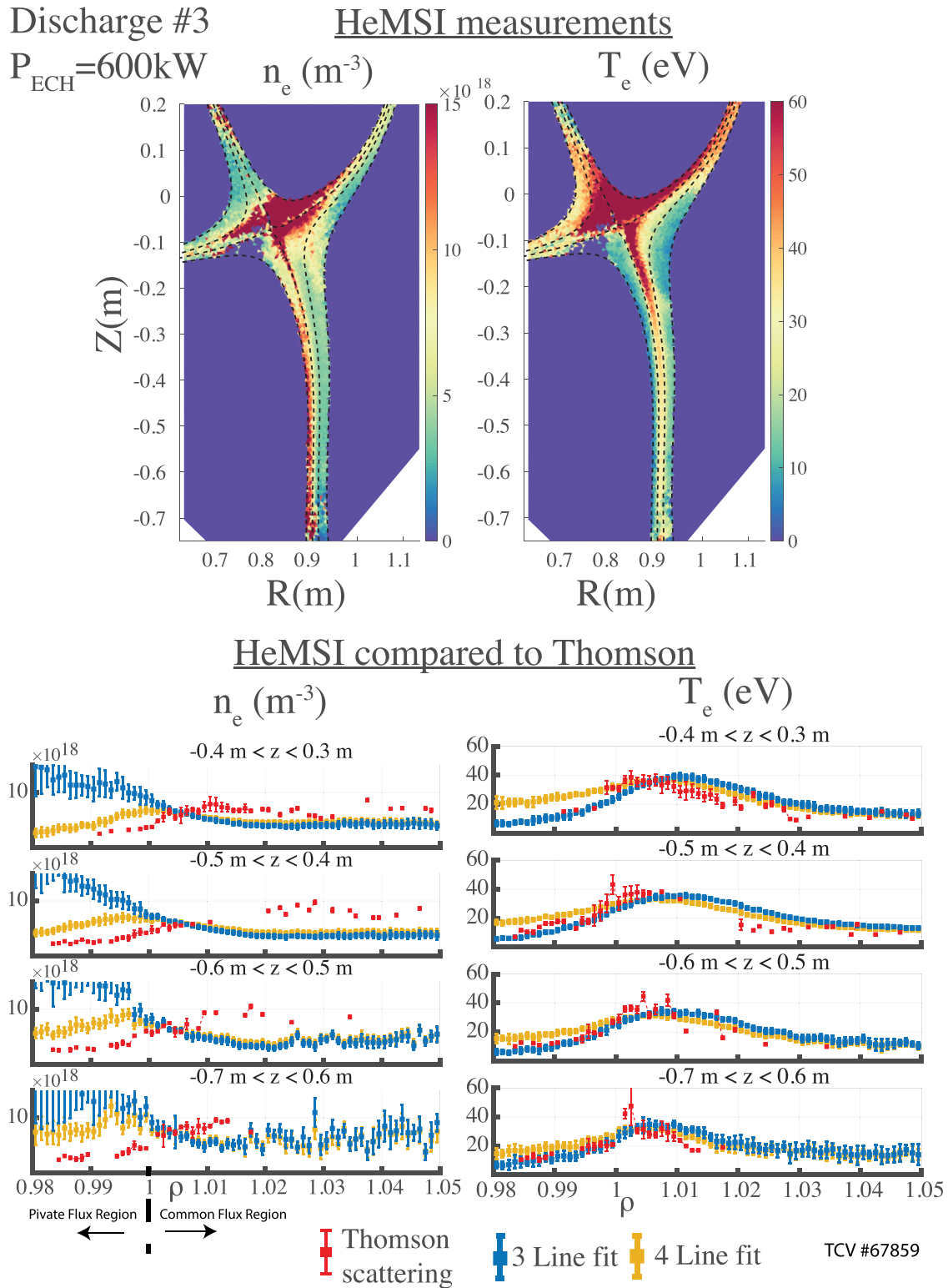


Figure 12. Discharge #3. Reversed-field helium plasma with $\bar{n}_e = 2.5 \times 10^{19} \text{ m}^{-3}$ with 600 kW of X2. HeMSI evaluations are shown with and without inclusion of 587 nm line.

However, the plasma species had no effect on the conditions of agreement between HeMSI and Thomson scattering measurements for ionizing plasmas. Violation of the QSE assumption is also not suspected because the $Lrt(\frac{728 \text{ nm}}{668 \text{ nm}})$ ratio (a singlet to singlet ratio) relaxes significantly faster than the $Lrt(\frac{728 \text{ nm}}{706 \text{ nm}})$ ratio.

7.1.6. Deuterium plasmas for $T_e < 10 \text{ eV}$. Discharge #6 demonstrates the disagreement observed between HeMSI and Thomson scattering for deuterium plasmas with $T_e < 10 \text{ eV}$. As displayed in figure 15, HeMSI greatly overestimates Thomson scattering’s measurements of T_e in the region where $T_e < 10 \text{ eV}$, i.e. $z < -0.4 \text{ m}$. However, $T_e \approx 10 \text{ eV}$ for $-0.4 \text{ m} < z < -0.3 \text{ m}$

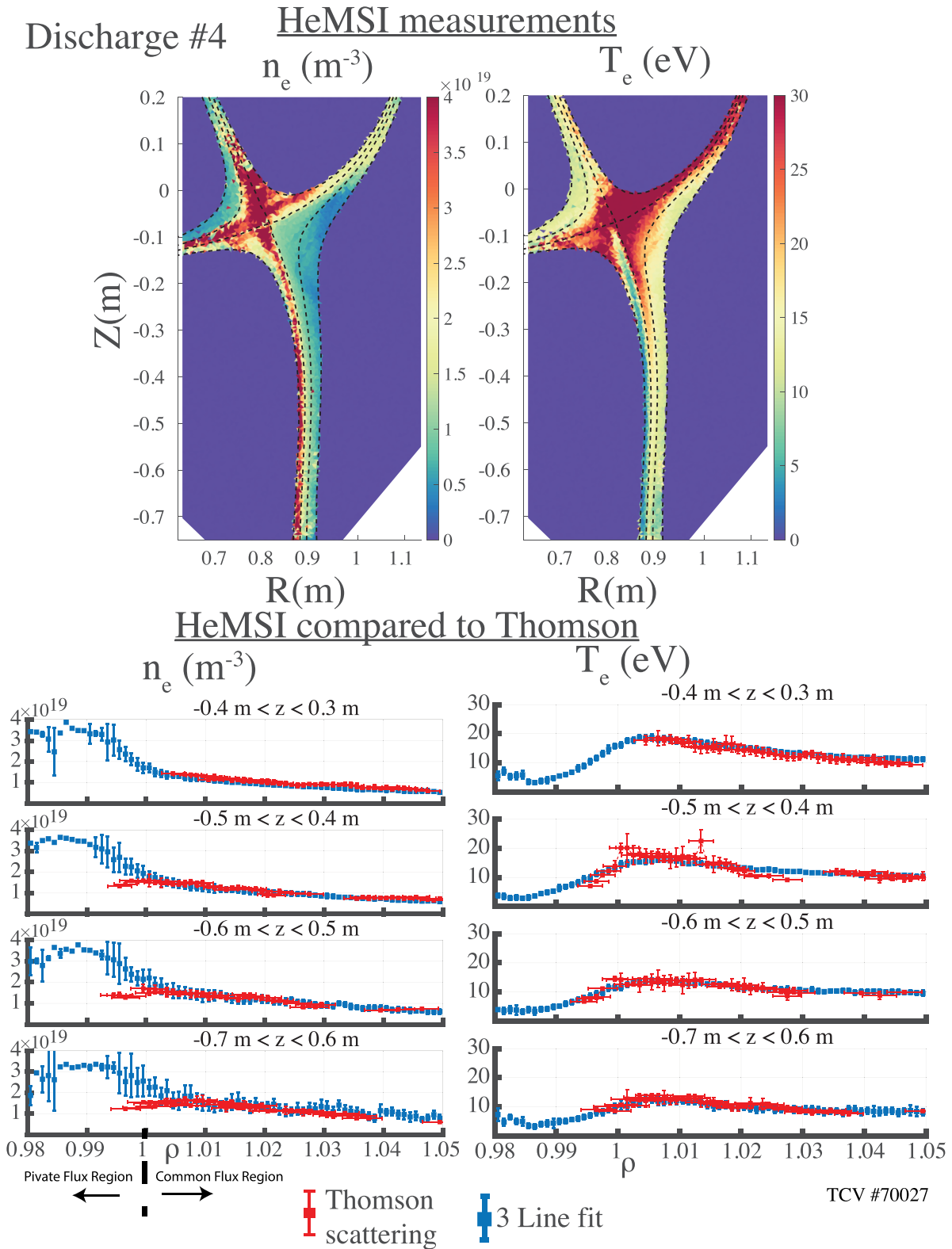


Figure 13. Discharge #4. Forward-field helium plasma with $\bar{n}_e = 7 \times 10^{19} m^{-3}$ and an unbaffled divertor. Images of the 587 line were not available in this discharge, so HeMSI evaluations do not include the 587 nm line.

and in this region, Thomson and HeMSI agree for both measurements. The ratio profiles within the region of disagreement for discharge #6 are shown in row 5 of figure 16. These profiles reveal that in the $T_e < 10 eV$ regime the measurements

of $Lrt(\frac{728nm}{706nm})$ are three times larger than the synthetic ratio. The larger $Lrt(\frac{728nm}{706nm})$ ratios cause the fitted T_e 's to be much higher than the actual T_e . This behavior was observed in all deuterium plasmas with $T_e < 10 eV$. However, while the CRM

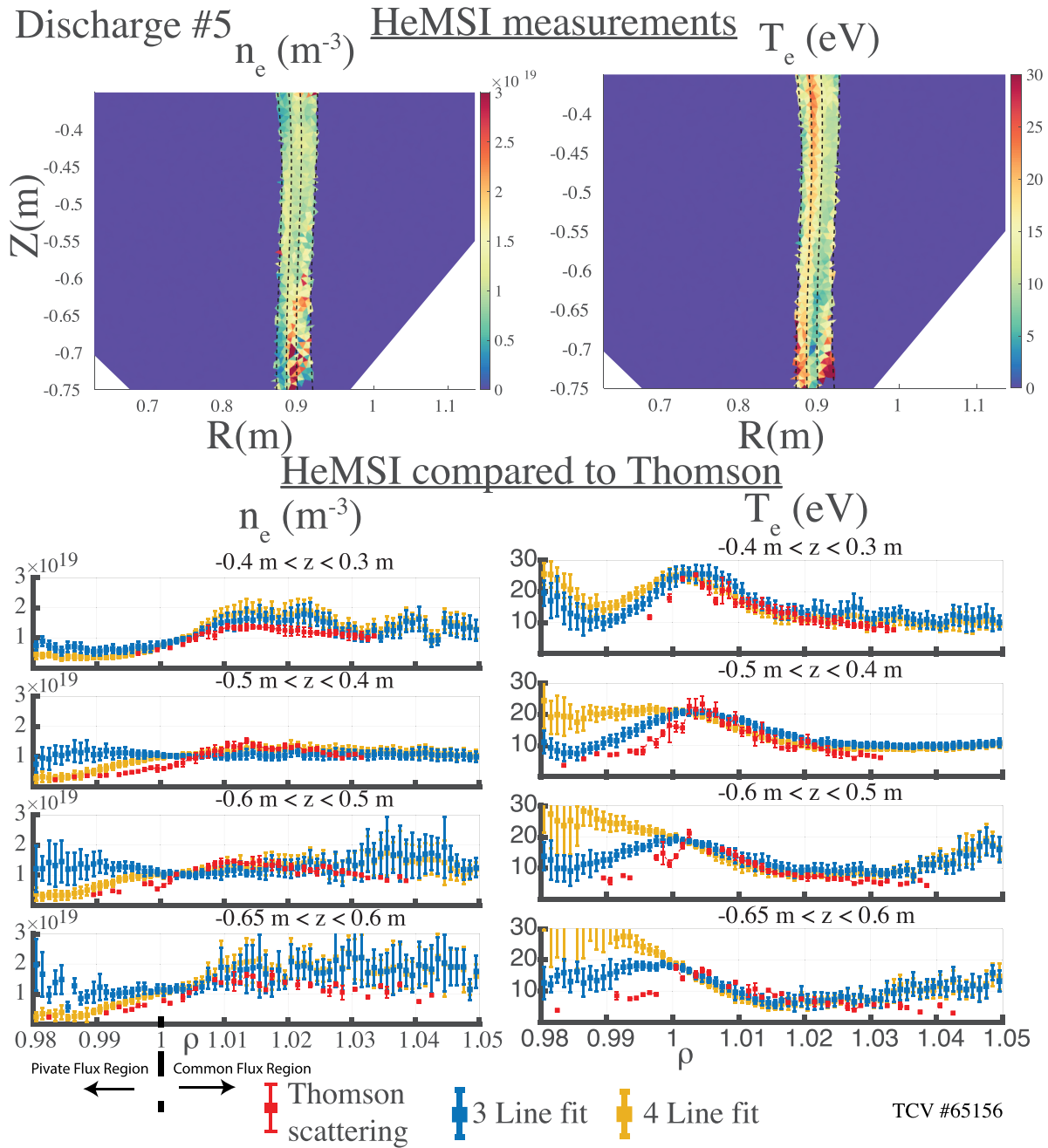


Figure 14. Discharge #5. Reversed-field deuterium plasma with $\bar{n}_e = 3 \times 10^{19} \text{ m}^{-3}$ and a baffled divertor. HeMSI evaluations are shown with and without inclusion of 587 nm line.

fails to produce agreement with T_e for $T_e < 10 \text{ eV}$, the n_e measurements compare favorably with those of Thomson scattering. This result is due to n_e 's strong dependence on $\text{Lrt}(\frac{728 \text{ nm}}{668 \text{ nm}})$ and weak dependence on $\text{Lrt}(\frac{728 \text{ nm}}{706 \text{ nm}})$ for $n_e > 1 \times 10^{19} \text{ m}^{-3}$.

To investigate this behavior, the discussion again returns to the neglected uncertainties. Similar to section 7.1.5, one ratio behaves as expected, while the other deviates; however, in this case, it is $\text{Lrt}(\frac{728 \text{ nm}}{706 \text{ nm}})$ that deviates. Thus, the discrepancy for $T_e < 10 \text{ eV}$ appears to be driven by the 706 nm line. Being driven by only one line, this disagreement is not thought to be an artifact of the camera's registration or the inversion process for the same reasons presented in section 7.1.5.

Again, the behavior appears to stem from incomplete modeling of He I and/or the plasma. As in section 7.1.5, the effects of toroidal asymmetries and filaments cannot be definitively dismissed. In regards to the CRM, the occurrence of this disagreement at lower temperatures suggests that the omission of EIR from the modeling be revisited. In section 7.2, this omission is shown to not be the source of the disagreement. Violation of the QSE assumption can also be refuted. Assume the helium is moving at 10 eV (the ion speed) which is a temperature 400 times greater than the 300 K assumed in figure 2(a). This temperature increase corresponds to a factor of 20 increase in velocity. This increase in velocity

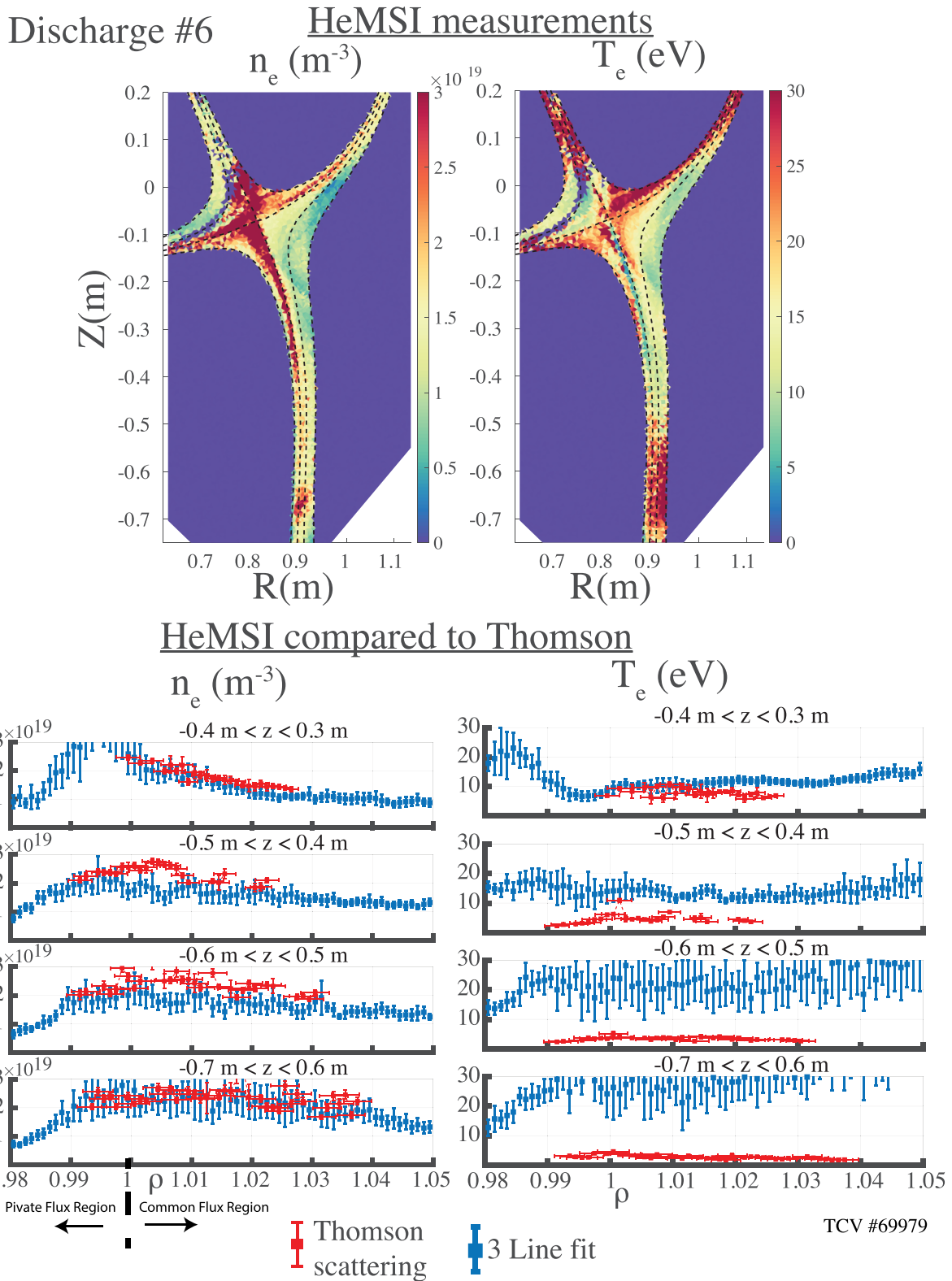


Figure 15. Discharge #6. Forward-field deuterium plasma with $\bar{n}_e = 6.5 \times 10^{19} m^{-3}$ and an unbaffled divertor. Images of the 587 line were not available in this discharge, so HeMSI evaluations do not include the 587 nm line.

corresponds to a $\lambda_{relax} = 4mm$ at $n_e = 1 \times 10^{19} m^{-3}$ and $T_e = 10eV$. The helium still only traverses a few millimeters in the poloidal plane before relaxing. Thus, violation of QSE cannot explain the behavior observed over the region of comparison, which is 4 cm in width.

However, the answer could also reside in molecular behaviors. The results for deuterium plasmas with $T_e < 10eV$ are consistent with the results from other He-H plasma experiments [19, 29–33]. In these reports, it was concluded or conjectured that molecular assisted recombination or

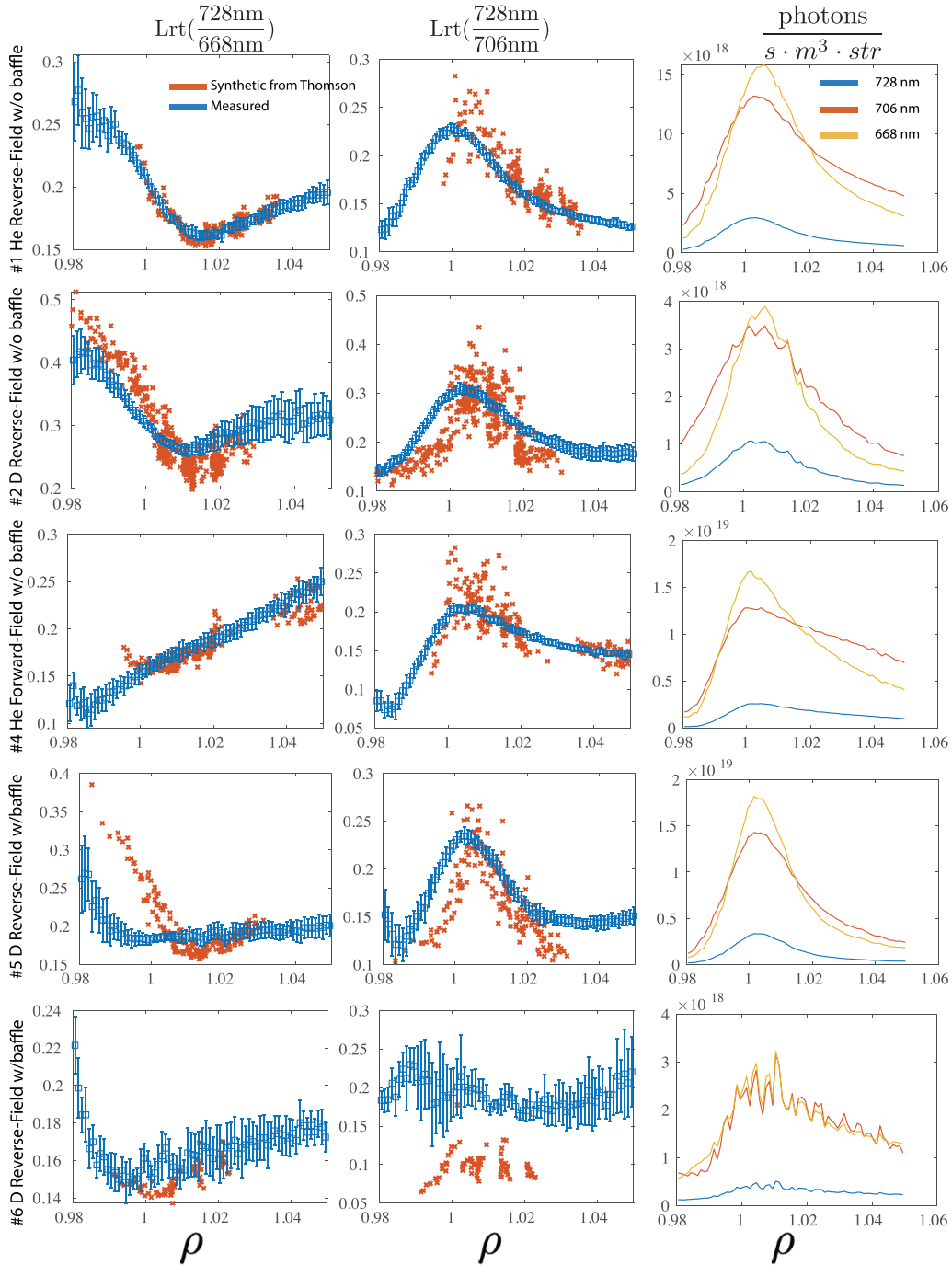


Figure 16. Each row displays line-ratio profiles from a different discharge for $-0.5\text{ m} < z < -0.4\text{ m}$. This presentation shows how the measurements of helium line ratios compare to the predictions created by applying G-CRM to the T_e and n_e Thomson scattering measurements.

molecular assisted dissociation processes were significantly affecting the He emission. It was shown in [29, 31] that deuterium can completely quench He^+ EIR processes for $1\text{ eV} \lesssim T_e \lesssim 6\text{ eV}$. In [19, 32], the addition of H_2 into a helium plasma was observed to perturb the ratios of singlet to triplet states, i.e. $\text{Lrt}(\frac{728\text{ nm}}{706\text{ nm}})$, but not greatly perturb singlet–singlet or triplet–triplet ratios. These results are consistent with the measurements reported here. Extending the CRM to consider molecular effects is beyond the scope of this work. However,

it will be shown in section 7.2 that $\text{Lrt}(\frac{728\text{ nm}}{706\text{ nm}})$ remains sensitive to T_e for $T_e < 10\text{ eV}$. This observation suggests that a more complete CRM may facilitate HeMSI measurements of T_e and n_e in this regime.

Irrespective of T_e and n_e diagnostic applications, understanding the helium spectral measurements in this $T_e < 10\text{ eV}$ regime may be of general interest to boundary physics. For example, the missing mechanism for helium emission could imply a collisional process that affects the transport of helium

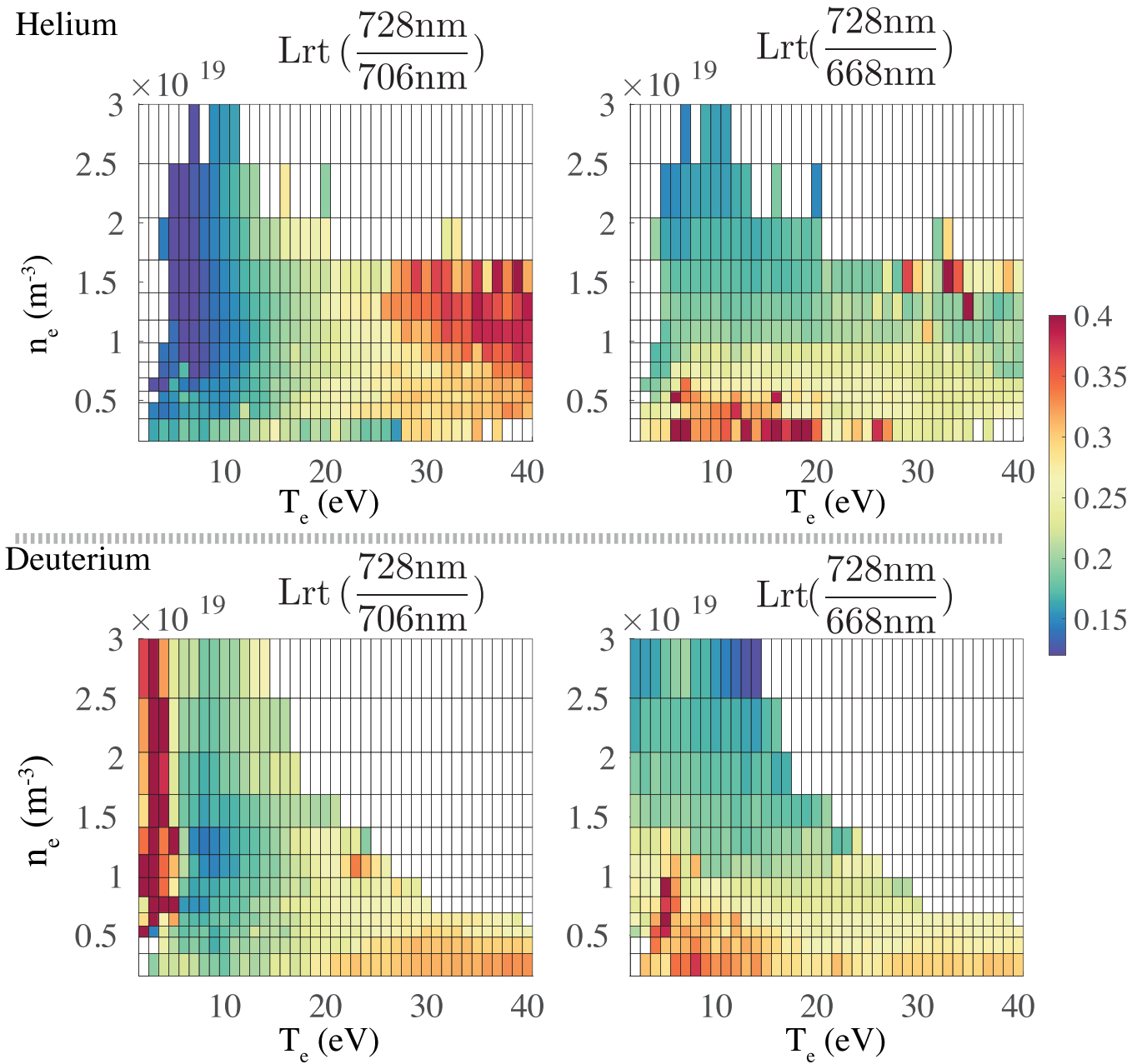


Figure 17. Average $Lrt\left(\frac{728\text{nm}}{706\text{nm}}\right)$ and $Lrt\left(\frac{728\text{nm}}{668\text{nm}}\right)$ measured at a given Thomson scattering value of T_e and n_e . Measurements restricted to the separatrix and common flux region.

ash in the boundary. Furthermore, understanding molecular processes is key to understanding detachment in TCV [82]. HeMSI measurement may assist with this understanding should molecular processes prove to be the missing components of the CRM.

7.2. Empirical trends

In this section, the HeMSI measurements in the common flux region are presented in aggregate. For each discharge, the HeMSI and Thomson scattering measurements in the common flux region were binned then averaged on (ρ, z) . For each

averaged HeMSI measurement, a corresponding Thomson scattering measurement was produced by linearly interpolating on the averaged Thomson scattering profile. In this section, the line-ratio measurements and HeMSI T_e and n_e measurements are presented as a function of these interpolated T_e and n_e Thomson scattering values. Measurements in the private flux region are omitted because HeMSI has poor precision in this region. All figures discussed in this section are segmented into majority helium and majority deuterium cases.

Beginning this overview, figure 17 presents the $Lrt\left(\frac{728\text{nm}}{706\text{nm}}\right)$ and $Lrt\left(\frac{728\text{nm}}{668\text{nm}}\right)$ measurements versus the Thomson scattering measured T_e and n_e . As expected, the measured $Lrt\left(\frac{728\text{nm}}{706\text{nm}}\right)$'s

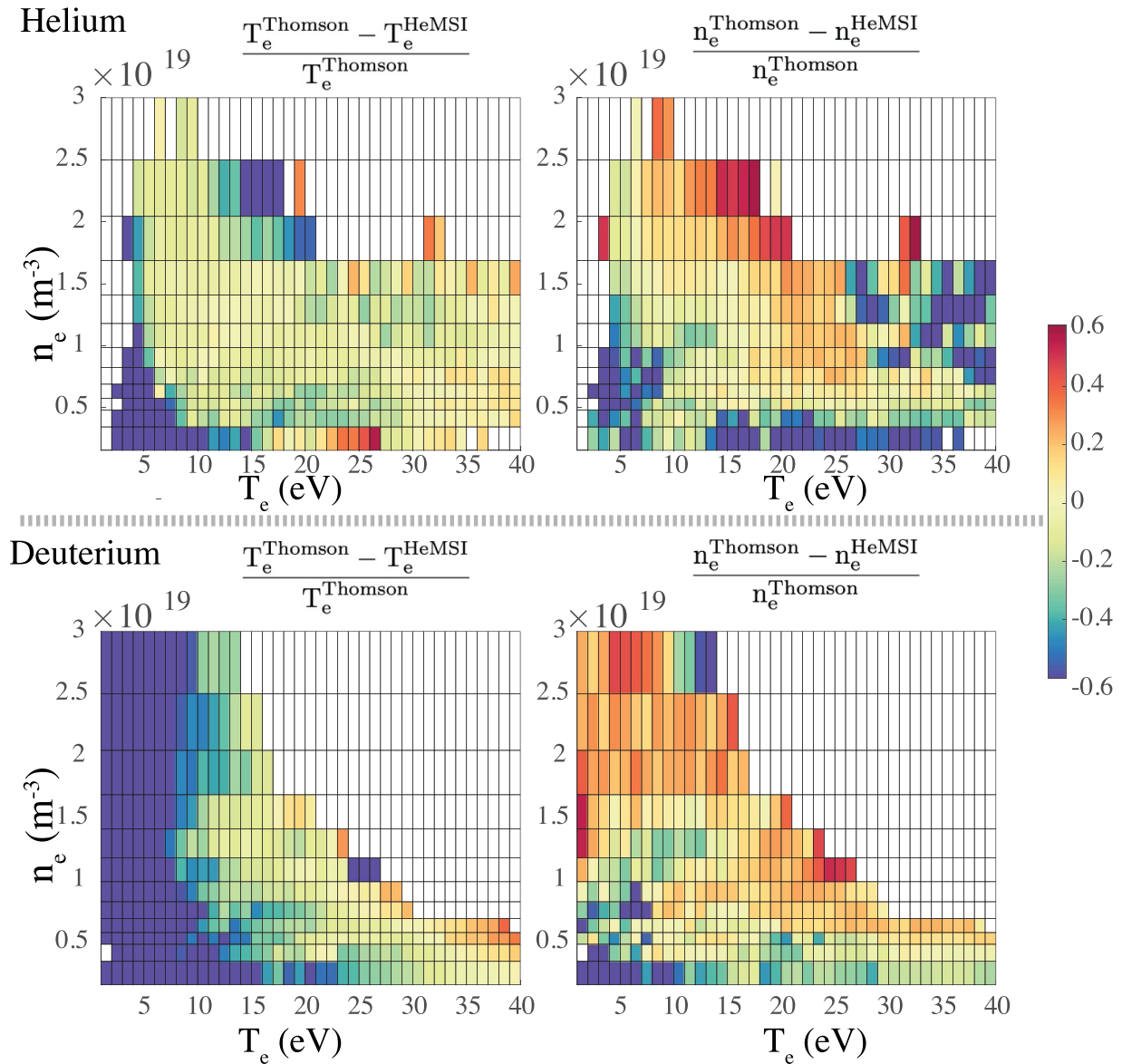


Figure 18. Comparison of T_e and n_e measured by HeMSI using G-CRM to that of Thomson scattering. Measurements restricted to the separatrix and common flux region.

are primarily a function of T_e and the measured $\text{Lrt}(\frac{728\text{nm}}{668\text{nm}})$'s are primarily a function of n_e . Note that the two ratios change smoothly over the parameter space.

Next, figure 18 presents the average fractional differences between HeMSI and Thomson scattering T_e and n_e measurements. As seen in figure 18, the HeMSI measurements of T_e are in strikingly good agreement with those of Thomson scattering for $T_e > 10\text{eV}$. Moreover, for majority helium plasmas, this good agreement continues for $T_e < 10\text{eV}$. The HeMSI measurements of n_e are in generally good agreement with Thomson scattering for $10\text{eV} < T_e < 20\text{eV}$ and $n_e < 1.75 \times 10^{19}\text{m}^{-3}$. For $21\text{eV} < T_e < 26\text{eV}$, there is a 20% systematic difference in the

n_e measurements between HeMSI and Thomson scattering for both helium and deuterium plasmas.

Similar to figures 18 and 19 displays the average fractional difference between the measured $\text{Lrt}(\frac{728\text{nm}}{706\text{nm}})$ and $\text{Lrt}(\frac{728\text{nm}}{668\text{nm}})$ ratios and those synthetically produced via Thomson scattering. The disagreements in n_e from figure 18 are seen in figure 19 to correspond to observations of $\text{Lrt}(\frac{728\text{nm}}{668\text{nm}})$ that are 20% smaller than what would be expected from G-CRM. The disagreement in $\text{Lrt}(\frac{728\text{nm}}{706\text{nm}})$ measurements for deuterium plasmas with $T_e < 10\text{eV}$ correspond to $\text{Lrt}(\frac{728\text{nm}}{706\text{nm}})$ observations that are 2 to 3 times smaller than what are expected.

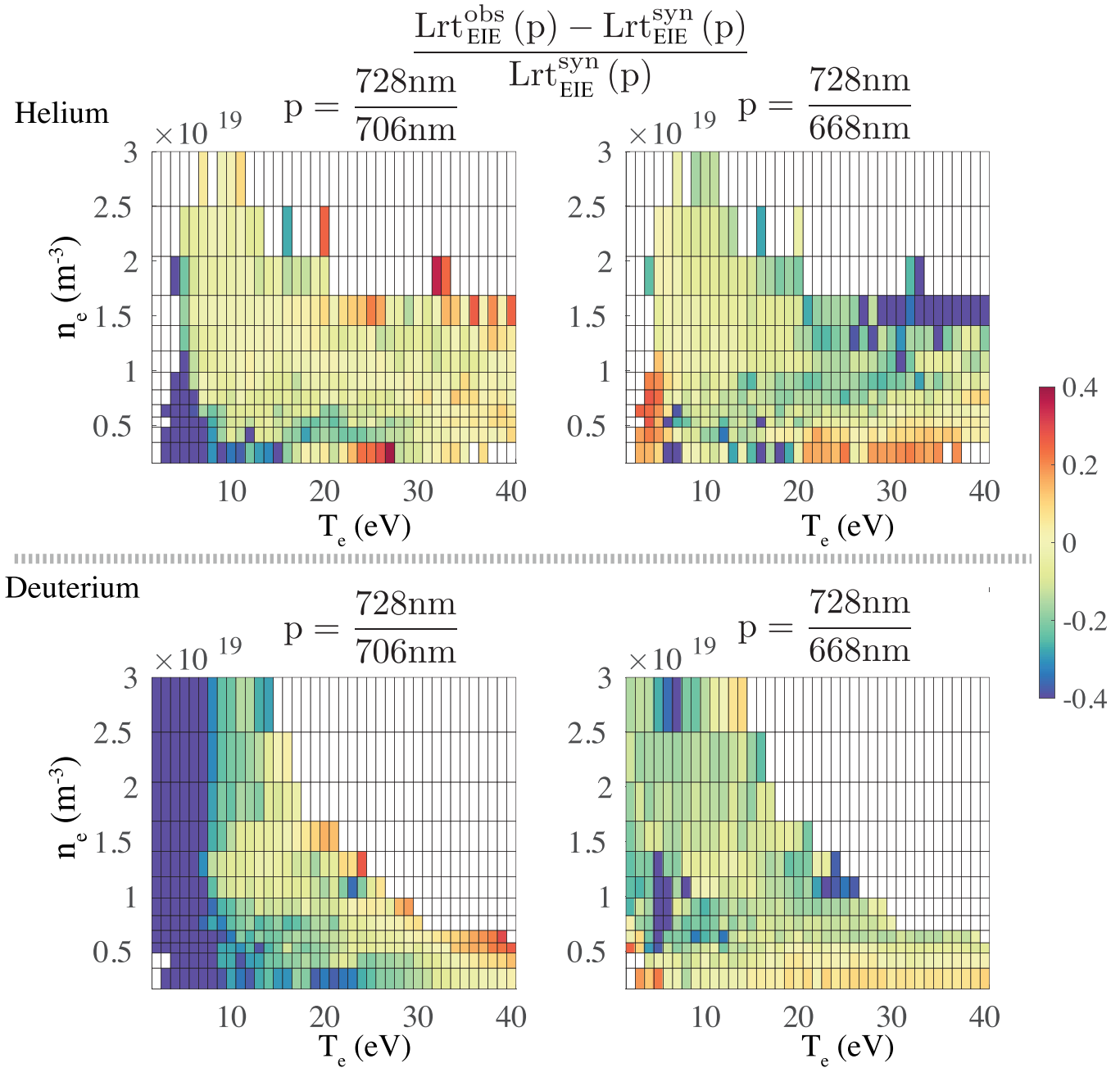


Figure 19. Comparison of $Lrt(\frac{728\text{nm}}{706\text{nm}})$ and $Lrt(\frac{728\text{nm}}{668\text{nm}})$ measurements to the expectation of an ionizing plasma produced from G-CRM and Thomson scattering measurements. Measurements restricted to the separatrix and common flux region.

The discrepancies at $T_e < 10\text{eV}$ are further explored in figure 20 which displays 1D box plots of $Lrt(\frac{728\text{nm}}{706\text{nm}})$ and $Lrt(\frac{728\text{nm}}{668\text{nm}})$ measurements versus the parameter to which they are most sensitive. On top of these box plots, the $Lrt(\frac{728\text{nm}}{706\text{nm}})$ and $Lrt(\frac{728\text{nm}}{668\text{nm}})$ predictions by G-CRM are plotted for constant n_e 's and T_e 's, respectively. The solid lines show predictions of the ratios for emission that is completely EIE driven, while the dashed lines correspond to emission that is driven entirely by

EIR. These box plots contain the same data that was shown in figure 19, but allow for trends to be more easily inferred. In particular, they highlight the disagreement observed for deuterium plasmas with $T_e < 10\text{eV}$. Prior to viewing figure 20, it could have been reasonably suspected that the disagreement for deuterium plasmas at $T_e < 10\text{eV}$ is caused by the omission of EIR in the fitting. However, assuming only EIR and EIE contribute to the emission, any $Lrt(\frac{728\text{nm}}{706\text{nm}})$ measurement must

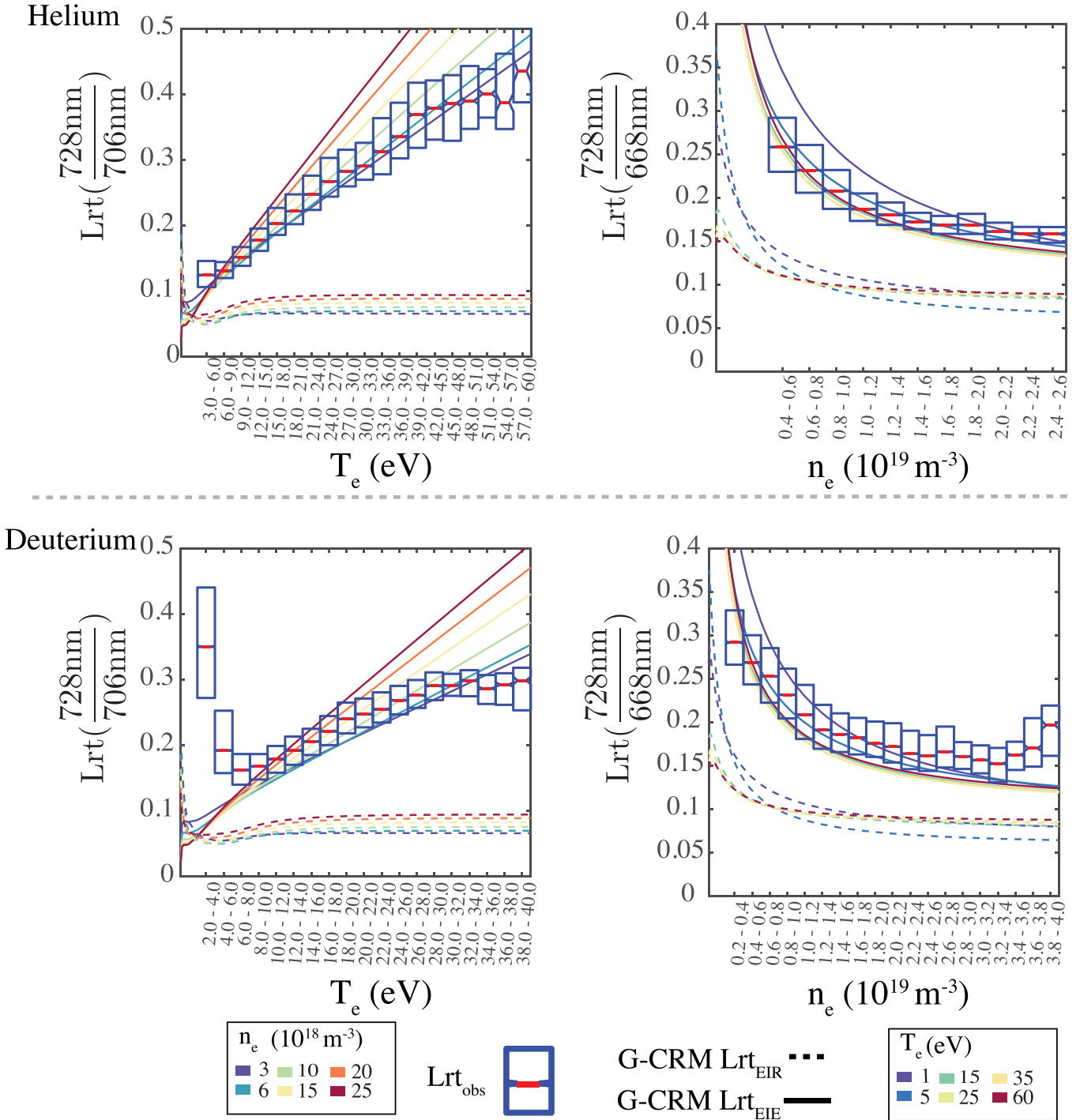


Figure 20. Box plots of $Lrt(\frac{728\text{nm}}{706\text{nm}})$ and $Lrt(\frac{728\text{nm}}{668\text{nm}})$ measurements versus the parameter to which they are most sensitive. The solid and dashed lines are produced by forward-modeling the line ratios with G-CRM. The solid line depicts the ratio of the EIE component, Lrt_{EIE} , whilst the dashed line depicts the ratio of the EIR component, Lrt_{EIR} .

Table 4. Description of discharges that are presented in this paper which applied HeMSI to a localized helium puff sent into a deuterium plasma.

Ref #	Fuel	$\bar{n}_e(10^{19}\text{m}^{-3})$	w 587nm	B_T Direction	Divertor type	Figure
#7	Deuterium	2	Yes	<i>rf</i>	Baffled	21
#8	Deuterium	3	No	<i>rf</i>	Baffled	22

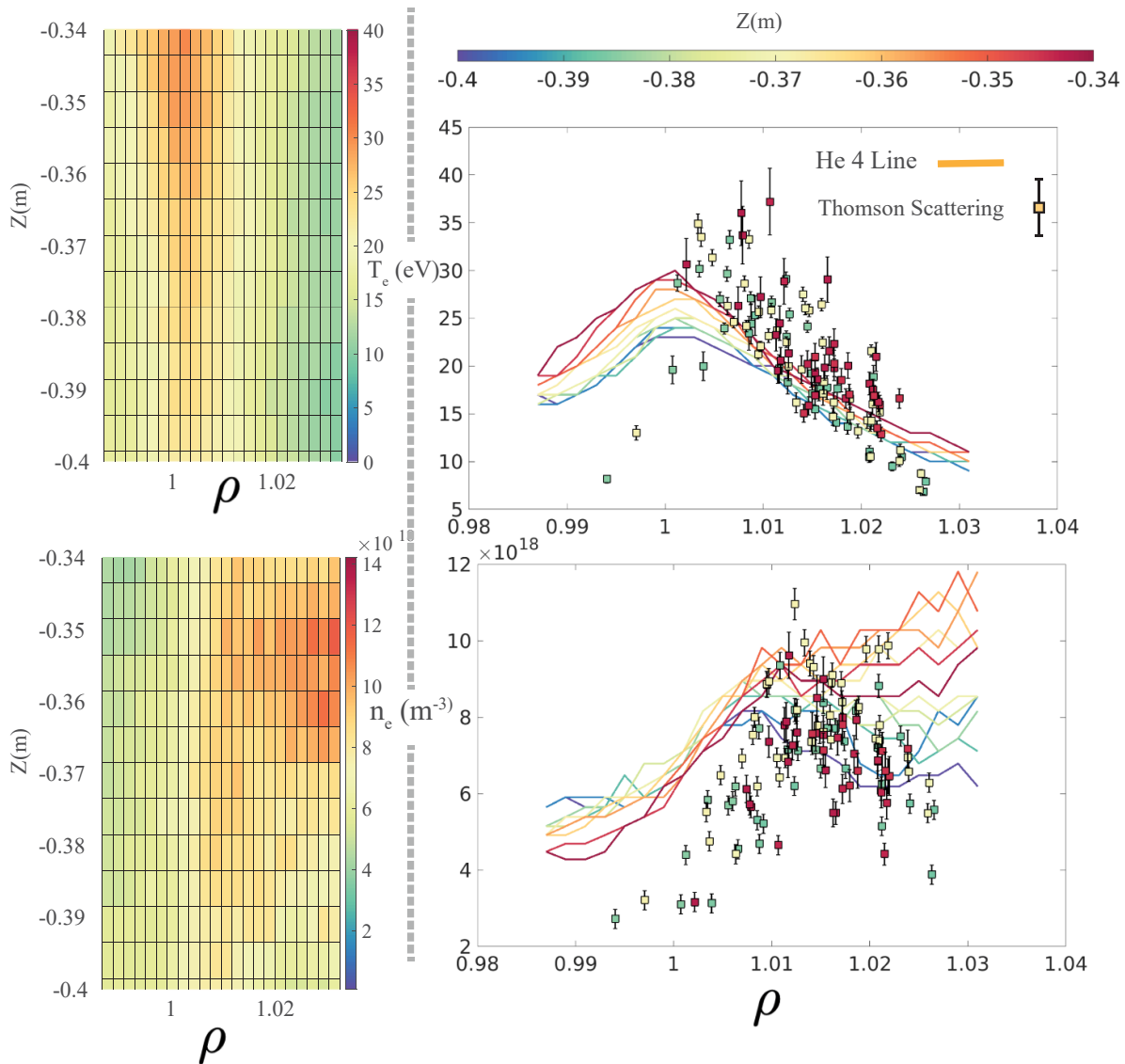


Figure 21. Comparison of HeMSI data collected from a localized puff into a reversed-field deuterium plasma at $\bar{n}_e = 2 \times 10^{19} \text{ m}^{-3}$. HeMSI fits include 587 nm line.

fall between what would be produced by fully EIE or fully EIR emission, i.e. between the solid and dashed lines in figure 20. However, in figure 20, the observed $\text{Lrt}(\frac{728 \text{ nm}}{706 \text{ nm}})$ is not only outside these bounds, but outside these bound on the side of the EIE bound, i.e. $\text{Lrt}(\frac{728 \text{ nm}}{706 \text{ nm}})_{\text{obs}} > \text{Lrt}(\frac{728 \text{ nm}}{706 \text{ nm}})_{\text{EIE}} > \text{Lrt}(\frac{728 \text{ nm}}{706 \text{ nm}})_{\text{EIR}}$. Thus, including EIR emission would only make the discrepancy between HeMSI and Thomson scattering worse.

Lastly, note for deuterium plasmas with $T_e < 10 \text{ eV}$ that the $\text{Lrt}(\frac{728 \text{ nm}}{706 \text{ nm}})$ retains a strong T_e dependence. Thus, the CRM may be able to be modified to accommodate this regime in the future.

7.3. Gas puff images

HeMSI measurements were also performed for localized gas puffs made into deuterium plasmas. Using a localized puff removed the need for an image inversion because the emission could be approximated as local. The results of the gas puff analysis were consistent with that from the inverted data. Good agreement was seen in the common flux region, but the agreement became worse near the separatrix going towards the private flux region. The results of the gas puff analysis for two discharges are shown in figures 21 and 22. The details of these two discharges are shown in table 4. The consistency between

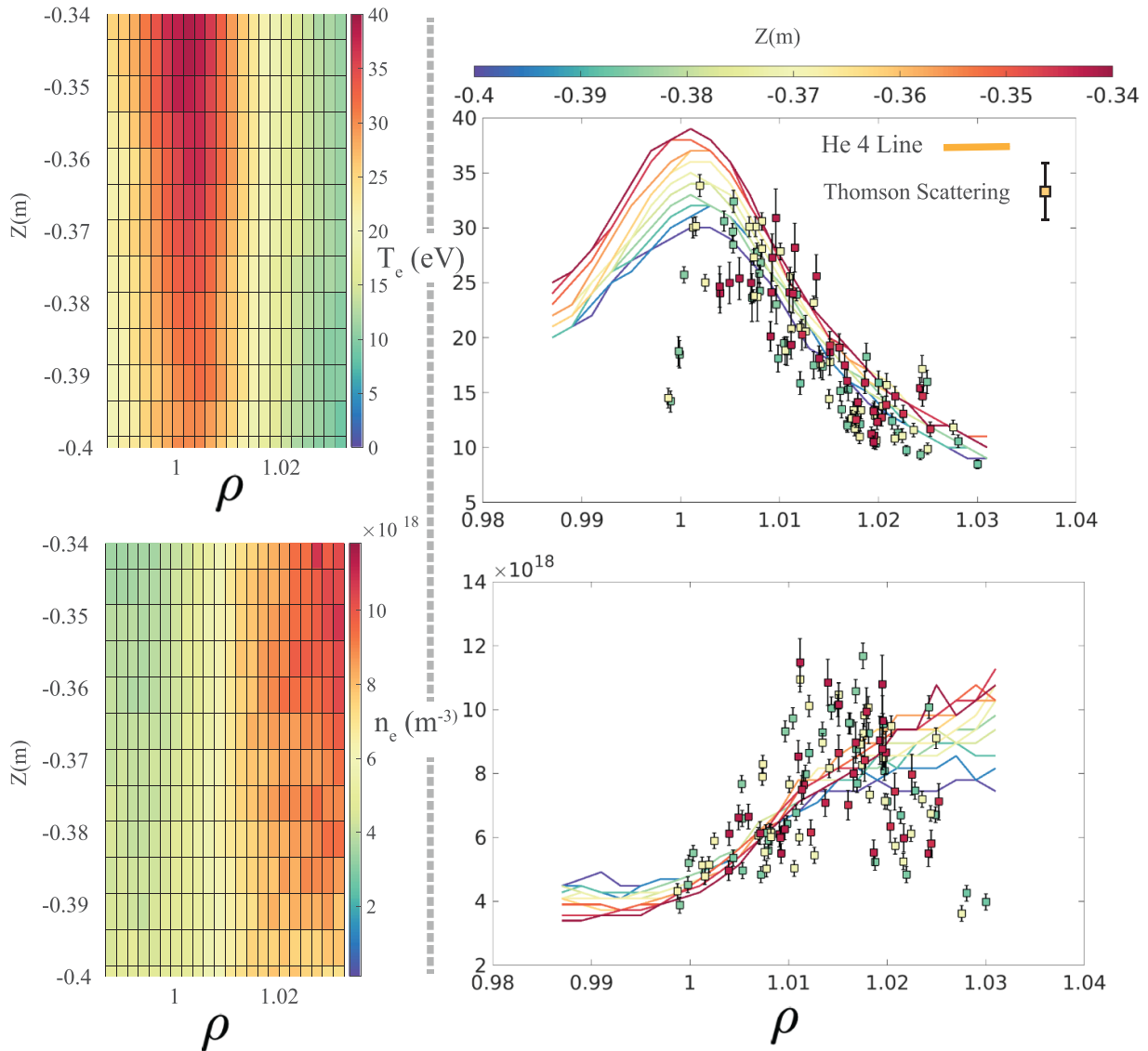


Figure 22. Comparison of HeMSI data collected from a localized puff into a reversed-field deuterium plasma at $\bar{n}_e = 3 \times 10^{19} \text{ m}^{-3}$. HeMSI fits include 587 nm line.

HLRS methodologies further bolsters confidence in the measurements made via inversion.

8. Conclusion

HeMSI was used to infer 2D poloidal maps of T_e and n_e at TCV with the Goto He CRM. These measurements were directly compared to co-local measurements from Thomson scattering. The measurements were found to be in good agreement in the common flux region of ionizing plasmas for:

- majority helium plasmas
 - * $5 \text{ eV} \leq T_e \leq 60 \text{ eV}$
 - * $2 \times 10^{18} \text{ m}^{-3} \leq n_e \leq 3 \times 10^{19} \text{ m}^{-3}$
- majority deuterium plasmas
 - * $10 \text{ eV} \leq T_e \leq 40 \text{ eV}$
 - * $2 \times 10^{18} \text{ m}^{-3} \leq n_e \leq 3 \times 10^{19} \text{ m}^{-3}$.

Breakdowns in this agreement were observed intermittently in the private flux region but observed consistently for deuterium plasmas with $T_e < 10 \text{ eV}$. It appears that the breakdowns in agreement are due to insufficiently complete modeling of the plasma and atomic physics and not errors in the diagnostic chain or inversion processes. The data reported here remains available for further analysis by more complete future codes.

This work is the first to directly compare Thomson scattering measurements of T_e and n_e to those generated from inverted He I emissivity profiles in a tokamak and exemplifies the wealth of quantitative information that can be gained from the inversion of high-resolution spectral images of passive emission. This paper will conclude by emphasizing the utility of these measurements, but first, the relevance of this work in the development of other multi-spectral imaging techniques will be noted.

The relatively recent implementation of high-resolution 10+ channel multi-spectral cameras for tokamak experiments [6] is giving rise to novel imaging applications at TCV [7, 8] and other experiments [83]. The ability to simultaneously quantify the density of multiple atomic and molecular states in 2D will likely facilitate climacteric insights into boundary physics. Consequently, this work is relevant to current and forthcoming multi-spectral imaging diagnostics as it demonstrates a need to be circumspect in the application of CRMs. As described in section 2.2, two sources of atomic data were considered in this work, G-CRM and A-CRM. While G-CRM produced excellent agreement with Thomson scattering for ionizing plasmas, A-CRM was found to significantly overestimate T_e . Furthermore, as described in 2.2, a He CRM consisting of only EIE and EIR processes does not describe emission from deuterium plasmas for $T_e < 10\text{eV}$. Thus, it is clear that inferences from CRMs must be validated against other, independent, diagnostics. This work can serve as a template for conducting such validations.

In conclusion, these innovative measurements provide unprecedented diagnostic coverage of T_e and n_e in the divertor and have immediate implications in furthering of divertor physics understanding. Extending this point, note that critical atomic and molecular processes that regulate the dynamics of particle and power balance in a divertor are either fully or partially determined by the local T_e and n_e . Radiative emission, electron-impact ionization, and EIR are examples of such processes. Thus, the T_e and n_e HeMSI profiles provide unique and innovative insights into particle and power balance in the volume of the divertor. As an example, the HeMSI measurements of T_e and n_e can be coupled with the absolute emissivity measurements of the He I and He II emissions to create 2D poloidal maps of He and He⁺ densities. Moreover, HeMSI measurements require only three spectral channels of the 10 or 6 available in the presented MANTIS diagnostic. Consequently, HeMSI can be used to contextualize the multi-spectral imaging analysis of other observed species such as deuterium [7, 8], carbon, nitrogen, etc. In cases where electron collisional processes are the dominant driver of spectral emission, this synergy will constrain—or fully determine—the populations of these other neutrals or ions across the poloidal plane.

When computationally modeling the plasma boundary in a tokamak, cross-field diffusion coefficients, D_{\perp} , and cross-field heat diffusivity, χ_{\perp} , are considered to be anomalous and matched to experimental measurements of T_e and n_e at the mid-plane. However, these coefficients affect the development of T_e and n_e profiles throughout the entire divertor volume. Therefore, by comparing T_e and n_e profiles with computational predictions, the HeMSI measurements will enhance investigation of transport within the plasma boundary.

These reported results prompt the use of HeMSI in future experiments at TCV where the boundary has a high concentration of He due to the inter-shot discharge cleaning cycle. HeMSI's exceptional spatial coverage is particularly well suited for TCV experiments that often implement a wide variety of divertor configurations such as single-null, double-null, super-X, and snowflake [5]. Going forward, application of HeMSI at TCV will provide innovative insights across these

extremely varied standard and alternative configurations in the pursuit of tokamak power exhaust solutions.

Acknowledgments

This work was supported in part by US DoE Grants DE-SC0020327 and DE-SC0010529. This work was supported in part by the Swiss National Science Foundation. This work has been carried out within the framework of the EUROfusion Consortium, funded by the European Union via the Euratom Research and Training Programme (Grant Agreement No. 101052200 EUROfusion). Views and opinions expressed are however those of the author(s) only and do not necessarily reflect those of the European Union or the European Commission. Neither the European Union nor the European Commission can be held responsible for them..

ORCID iDs

B.L. Linehan  <https://orcid.org/0000-0001-9133-1662>
 A. Perek  <https://orcid.org/0000-0002-4117-0298>
 B.P. Duval  <https://orcid.org/0000-0001-7783-129X>
 F. Bagnato  <https://orcid.org/0000-0002-1228-6005>
 O. Février  <https://orcid.org/0000-0002-9290-7413>
 E. Flom  <https://orcid.org/0000-0002-9284-9380>
 S. Gorno  <https://orcid.org/0000-0003-0524-7283>
 M. Goto  <https://orcid.org/0000-0002-9160-682X>
 L. Martinelli  <https://orcid.org/0000-0002-7618-1077>
 A. Mathews  <https://orcid.org/0000-0002-6363-7055>
 J. Muñoz-Burgos  <https://orcid.org/0000-0002-8089-7422>
 N. Offeddu  <https://orcid.org/0000-0002-0534-1993>
 D.S. Oliveira  <https://orcid.org/0000-0002-6888-2594>
 H. Reimerdes  <https://orcid.org/0000-0002-9726-1519>
 D. Reiter  <https://orcid.org/0000-0001-5635-7103>
 O. Schmitz  <https://orcid.org/0000-0002-9580-9149>
 J.L. Terry  <https://orcid.org/0000-0003-4255-5509>
 C. Theiler  <https://orcid.org/0000-0003-3926-1374>
 C.K. Tsui  <https://orcid.org/0000-0002-7346-8312>
 B. Vincent  <https://orcid.org/0000-0001-5420-6002>
 T. Wijkamp  <https://orcid.org/0000-0003-3110-8682>
 C. Wüthrich  <https://orcid.org/0000-0001-7548-2452>
 W. Zholobenko  <https://orcid.org/0000-0002-2624-0251>

References

- [1] Zohm H., Militello F., Morgan T.W., Morris W., Reimerdes H. and Siccino M. 2021 The EU strategy for solving the DEMO exhaust problem *Fusion Eng. Des.* **166** 112307
- [2] Coda S. *et al* 2017 Overview of the TCV tokamak program: scientific progress and facility upgrades *Nucl. Fusion* **57** 102011
- [3] Reimerdes H. *et al* 2017 TCV experiments towards the development of a plasma exhaust solution *Nucl. Fusion* **57** 126007
- [4] Labit B. *et al* 2017 Experimental studies of the snowflake divertor in TCV *Nucl. Mater. Energy* **12** 1015–19

- [5] Theiler C. et al 2017 Results from recent detachment experiments in alternative divertor configurations on TCV *Nucl. Fusion* **57** 072008
- [6] Perek A. et al 2019 Mantis: a real-time quantitative multispectral imaging system for fusion plasmas *Rev. Sci. Instrum.* **90** 123514
- [7] Perek A. et al 2021 Measurement of the 2d emission profiles of hydrogen and impurity ions in the TCV divertor *Nucl. Mater. Energy* **26** 100858
- [8] Perek A. et al (the EUROfusion MST1 Team and the TCV Team) 2022 A spectroscopic inference and SOLPS-ITER comparison of flux-resolved edge plasma parameters in detachment experiments on TCV *Nucl. Fusion* **62** 096012
- [9] Zholobenko W., Rack M., Reiter D., Goto M., Feng Y., Küppers B. and Börner P. 2018 Synthetic helium beam diagnostic and underlying atomic data *Nucl. Fusion* **58** 126006
- [10] Zholobenko W., Rack M. and Reiter D. 2018 Development and evaluation of a synthetic helium beam diagnostic for Wendelstein 7-X *Technical Report Juel-4407* Jülich (available at: <https://juser.fz-juelich.de/record/844035>)
- [11] Goto M. 2003 Collisional-radiative model for neutral helium in plasma revisited *J. Quant. Spectrosc. Radiat. Transfer* **76** 331–44
- [12] Cunningham S.P., Beaver R.J. and Waugh R.C. 1955 US atomic energy commission rep WASH-289 p 279
- [13] Wendler D., Dux R., Fischer R., Griener M., Wolfrum E., Birkenmeier G. and Stroth U. 2022 Collisional radiative model for the evaluation of the thermal helium beam diagnostic at ASDEX upgrade *Plasma Phys. Control. Fusion* **64** 045004
- [14] Griener M., Wolfrum E., Cavedon M., Dux R., Rohde V., Sochor M., Muñoz B.J.M., Schmitz O. and Stroth U. 2018 *Rev. Sci. Instrum.* **89** 10D102
- [15] Kajita S., Nishijima D., Fujii K., Akkermans G. and Van Der Meiden H. 2021 Application of multiple regression for sensitivity analysis of helium line emissions to the electron density and temperature in Magnum-PSI *Plasma Phys. Control. Fusion* **63** 055018
- [16] Nishijima D., Kajita S. and Tynan G.R. 2021 Machine learning prediction of electron density and temperature from He I line ratios *Rev. Sci. Instrum.* **92** 023505
- [17] Schmitz O. et al 2008 Status of electron temperature and density measurement with beam emission spectroscopy on thermal helium at TEXTOR *Plasma Phys. Control. Fusion* **50** 115004
- [18] Goto M. and Sawada K. 2014 Determination of electron temperature and density at plasma edge in the Large Helical Device with opacity-incorporated helium collisional-radiative model *J. Quant. Spectrosc. Radiat. Transfer* **137** 23–28
- [19] Iida Y., Kado S. and Tanaka S. 2013 On the application of He I collisional-radiative model to the He-H–2 mixture plasmas in MAP-II divertor simulator *J. Nucl. Mater.* **438** S1237–40
- [20] Okamoto A., Kado S., Sawada K., Kuwahara Y., Iida Y. and Tanaka S. 2007 Contribution of hydrogen molecular assisted recombination processes to population of hydrogen atom in divertor simulator MAP-II *J. Nucl. Mater.* **363–365** 395–9
- [21] Ma S., Howard J., Blackwell B.D. and Thapar N. 2012 Measurements of electron density and temperature in the H-1 heliac plasma by helium line intensity ratios *Rev. Sci. Instrum.* **83** 033102
- [22] De La Cal E. and Guasp J. 2011 Two-dimensional imaging of edge plasma electron density and temperature by the passive helium emission ratio technique in TJ-II *Plasma Phys. Control. Fusion* **53** 085006
- [23] Lisgo S., Börner P., Counsell G.F., Dowling J., Kirk A., Scannell R., O’Mullane M. and Reiter D. 2009 Interpretation of spatially resolved helium line ratios on MAST *J. Nucl. Mater.* **390–391** 1078–80
- [24] Kajita S., Ohno N., Takamura S. and Nakano T. 2006 Comparison of He I line intensity ratio method and electrostatic probe for electron density and temperature measurements in NAGDIS-II *Phys. Plasmas* **13** 1–9
- [25] Carraro L., De Pol G., Puiatti M.E., Sattin F., Scarin P. and Valisa M. 2000 Edge temperature and density measurements with a thermal helium beam in the RFX reversed field pinch *Plasma Phys. Control. Fusion* **42** 1–14
- [26] Field A.R., Carolan P.G., Conway N.J. and O’Mullane M.G. 1999 Optimized instrumentation for edge T_e and n_e measurements on COMPASS-D tokamak from He I line intensity ratios *Rev. Sci. Instrum.* **70** 355–8
- [27] Kubo H., Goto M., Takenaga H., Kumagai A., Sugie T., Sakurai S., Asakura N., Higashijima S. and Sakasai S.A.K.A.S.A.I. 1999 Study of intensity ratios of He I Line (668 nm, 706 nm and 728 nm) for measurement of electron temperature and density in JT-60U divertor plasma *J. Plasma Fusion Res.* **75** 945–66
- [28] Davies S.J. et al 1997 Parallel electron temperature and density gradients measured in the JET MkI divertor using thermal helium beams *J. Nucl. Mater.* **241–243** 426–32
- [29] Ohno N., Ezumi N., Takamura S., Krasheninnikov S.I. and Pigarov A.Y. 1998 Experimental evidence of molecular activated recombination in detached recombining plasmas *Phys. Rev. Lett.* **81** 818–21
- [30] Nishijima D., Wenzel U., Ohsumi K., Ohno N., Uesugi Y. and Takamura S. 2002 Characteristics of detached plasmas associated with electron-ion and molecular assisted recombinations in NAGDIS-II *Plasma Phys. Control. Fusion* **44** 597–610
- [31] Cai L., Tynan G.R. and Hollmann E.M. 2008 Evidence for molecular-assisted recombination of He+ from particle balance measurements in helium-hydrogen mixture plasmas in PISCES-A *Phys. Plasmas* **15** 102505
- [32] Kajita S., Suzuki K., Tanaka H. and Ohno N. 2018 Helium line emission spectroscopy in recombining detached plasmas *Phys. Plasmas* **25** 063303
- [33] Nishijima D., Doerner R.P., Baldwin M.J., Hollmann E.M., Seraydarian R.P. and Ueda Y. 2007 Spectroscopic determination of the singly ionized helium density in low electron temperature plasmas mixed with helium in a linear divertor plasma simulator *Phys. Plasmas* **14** 103509
- [34] Bates D., Kingston A. and McWhirter R. 1962 Recombination between electrons and atomic ions I. Optically thin plasmas *Proc. R. Soc. A* **301** 355–61
- [35] Fujimoto T. 2004 *Plasma Spectroscopy (International Series of Monographs on Physics)* (Oxford: Oxford University Press)
- [36] Summers H.P., Dickson W.J., O’Mullane M.G., Badnell N.R., Whiteford A.D., Brooks D.H., Lang J., Loch S.D. and Griffin D.C. 2006 Ionization state, excited populations and emission of impurities in dynamic finite density plasmas: I. The generalized collisional-radiative model for light elements *Plasma Phys. Control. Fusion* **48** 263–93
- [37] Fujimoto T. 1979 A collisional-radiative model for helium and its application to a discharge plasma *J. Quant. Spectrosc. Radiat. Transfer* **21** 439–55
- [38] Muñoz B.J.M., Schmitz O., Loch S.D. and Ballance C.P. 2012 Hybrid time dependent/independent solution for the He I line ratio temperature and density diagnostic for a thermal helium beam with applications in the scrape-off layer-edge regions in tokamaks *Phys. Plasmas* **19** 012501
- [39] Drake G.W.F. and Yan Z.C. 1992 Energies and relativistic corrections for the Rydberg states of helium: variational results and asymptotic analysis *Phys. Rev. A* **46** 2378–409

- [40] Kramida A., Yu R., Reader J. and (NIST ASD Team) 2021 NIST atomic spectra database (ver. 5.9) (available at: <https://physics.nist.gov/asd>) (Accessed 9 April 2017) (Gaithersburg, MD: National Institute of Standards and Technology)
- [41] Ralchenko Y., Janev R.K., Kato T., Fursa D.V., Bray I. and de Heer F.J. 2008 Electron-impact excitation and ionization cross sections for ground state and excited helium atoms *At. Data Nucl. Data Tables* **94** 603–22
- [42] Ballance C.P., Griffin D.C., Loch S.D., Boivin R.F. and Pindzola M.S. 2006 Collisional-radiative calculations of He line emission in low-temperature plasmas *Phys. Rev. A* **74** 1–8
- [43] Burgess A. and Summers H.P. 1976 The recombination and level populations of ions-I HYDROGEN AND HYDROGENIC IONS *Mon. Not. R. Astron. Soc.* **174** 345–91
- [44] Summers H. P. 2004 The ADAS User Manual, version 2.6 (available at: <http://www.adas.ac.uk>)
- [45] Sasaki S., Takamura S., Watanabe S., Masuzaki S., Kato T. and Kadota K. 1996 Helium I line intensity ratios in a plasma for the diagnostics of fusion edge plasmas *Rev. Sci. Instrum.* **67** 3521–9
- [46] Fujimoto M. 1997 T collisional-radiative model for neutral helium in plasma: excitation cross section and singlet-triplet wavefunction mixing (*NIFS-DATA-43*)
- [47] Goto M. and Fujimoto T. 1997 Collisional-radiative model for helium and its application to a tokamak plasma *Fusion Eng. Des.* **34–35** 759–62
- [48] Iida Y., Kado S., Okamoto A. and Kajita S. 2006 Effect of radiation trapping on an He I CR model for a divertor simulator MAP-II *New research on atomic and molecular processes and the increasing applications to plasmas, science and technology. Proc. Joint Meetings of ITC-14 and ICAMDATA 2004. (October 5 - 8, 2004, Toki, Japan)* vol 7 pp 123–6
- [49] Stotler D.P., Boedo J., LeBlanc B., Maqueda R.J. and Zweben S.J. 2007 Progress towards the validation of models of the behavior of neutral helium in gas puff imaging experiments *J. Nucl. Mater.* **363–365** 686–92
- [50] Rosmej F.B., Ohno N., Takamura S. and Kajita S. 2008 Fluctuating helium emission in optically thick divertor plasmas *Contrib. Plasma Phys.* **48** 243–8
- [51] Kajita S., Nishijima D., Hollmann E.M. and Ohno N. 2009 Ray tracing simulation for radiation trapping of the He I resonance transitions in a linear plasma device *Phys. Plasmas* **16** 063303
- [52] Iida Y., Kado S., Muraki A. and Tanaka S. 2010 Application of optical emission spectroscopy for He I considering the spatial structure of radiation trapping in MAP-II divertor simulator *Rev. Sci. Instrum.* **81** 10E511
- [53] Iida Y., Kado S. and Tanaka S. 2010 Calculation of spatial distribution of optical escape factor and its application to He I collisional-radiative model *Phys. Plasmas* **17** 123301
- [54] Sawada K., Yamada Y., Miyachika T., Ezumi N., Iwamae A. and Goto M. 2010 Collisional-radiative model for spectroscopic diagnostic of optically thick Helium plasma *Plasma Fusion Res.* **5** 001
- [55] Kajita S. and Ohno N. 2011 Practical selection of emission lines of He I to determine the photon absorption rate *Rev. Sci. Instrum.* **82** 023501
- [56] Ma S., Howard J. and Thapar N. 2011 Relations between light emission and electron density and temperature fluctuations in a helium plasma *Phys. Plasmas* **18** 083301
- [57] Kajita S. et al 2017 Behavior of 23S metastable state He atoms in low-temperature recombining plasmas *Phys. Plasmas* **24** 073301
- [58] Lee W., Park K. and Oh C.H. 2017 Study on the radiative excitation rate coefficient of collisional radiative model *Phys. Plasmas* **24** 063510
- [59] Lee W. and Oh C.H. 2018 Optical diagnostics of helium recombining plasmas with collisional radiative model *Phys. Plasmas* **25** 113504
- [60] Kajita S., Akkermans G., Fujii K., Van Der Meiden H. and Van De Sanden M.C. 2020 Emission spectroscopy of He lines in high-density plasmas in Magnum-PSI *AIP Adv.* **10** 025225
- [61] Nishijima D., Patino M.I. and Doerner R.P. 2020 New application of hyperspectral imaging to steady-state plasma observations *Rev. Sci. Instrum.* **91** 083501
- [62] Mathews A., Terry J.L., Baek S.G., Hughes J.W., Kuang A.Q., LaBombard B., Miller M.A., Zweben S.J., Stotler D., Reiter D., Zholobenko W. and Goto M. 2022 Deep modelling of plasma and neutral fluctuations from gas puff turbulence imaging (arXiv:2201.09988)
- [63] Muñoz B.J.M., Schmitz O., Unterberg E.A., Loch S.D. and Ballance C.P. 2011 Implementation of a new atomic basis for the He I equilibrium line ratio technique for electron temperature and density diagnostic in the SOL for H-mode plasmas in DIII-D *J. Nucl. Mater.* **415** 1155–8
- [64] Hollmann E.M., Brandt C., Hudson B., Kumar D., Nishijima D. and Pigarov A.Y. 2013 Investigation of mechanisms for He-I emission radial profile broadening in a weakly ionized cylindrical helium plasma with recombining edge *Phys. Plasmas* **20** 093303
- [65] Muñoz B.J.M., Barbui T., Schmitz O., Stutman D. and Tritz K. 2016 Time-dependent analysis of visible helium line-ratios for electron temperature and density diagnostic using synthetic simulations on NSTX-U *Rev. Sci. Instrum.* **87** 1–5
- [66] Muñoz B.J.M., Agostini M., Scarin P., Stotler D.P., Unterberg E.A., Loch S.D., Schmitz O., Tritz K. and Stutman D. 2016 Evaluation of thermal helium beam and line-ratio fast diagnostic on the National Spherical Torus Experiment-Upgrade *Phys. Plasmas* **23** 53302
- [67] Griener M. et al 2018 Qualification and implementation of line ratio spectroscopy on helium as plasma edge diagnostic at ASDEX Upgrade *Plasma Phys. Control. Fusion* **60** 025008
- [68] Flom E. et al 2022 Bayesian modeling of collisional-radiative models applicable to thermal helium beam plasma diagnostics *Nucl. Mater. Energy* **33** 101269
- [69] Wüthrich C.T. et al 2022 X-point and divertor filament dynamics from gas puff imaging on TCV *Nucl. Fusion* **62** 106022
- [70] Silburn S. et al 2021 Version 2.7.0. 2021 *Calcam* (available at: <http://doi.org/10.5281/zenodo.4698377>)
- [71] Andersen A.H. and Kak A.C. 1984 Simultaneous algebraic reconstruction technique (SART): a superior implementation of the art algorithm *Ultrason. Imaging* **6** 81–94
- [72] Nakano T., Kubo H., Asakura N., Shimizu K., Kawashima H. and Higashijima S. 2009 Radiation process of carbon ions in JT-60U detached divertor plasmas *J. Nucl. Mater.* **390–391** 255–8
- [73] Blanchard P. et al 2019 Thomson scattering measurements in the divertor region of the TCV tokamak plasmas *J. Instrum.* **14** C10038
- [74] Martinelli L. et al 2022 Implementation of high-resolution spectroscopy for ion (and electron) temperature measurements of the divertor plasma in the tokamak á configuration variable *Rev. Sci. Instrum.* **93** 123505
- [75] Irons F.E. 1979 The escape factor in plasma spectroscopy-I. The escape factor defined and evaluated *J. Quant. Spectrosc. Radiat. Transfer* **22** 1–20
- [76] Wensing M., Loizu J., Reimerdes H., Duval B.P. and Wischmeier M. 2020 X-point potential well formation in

- diverted tokamaks with unfavorable magnetic field direction
Nucl. Fusion **60** 1–8
- [77] Jaervinen A. *et al* 2017 Interpretations of the impact of cross-field drifts on divertor flows in DIII-D with UEDGE
Nucl. Mater. Energy **12** 1136–40
- [78] Wensing M., Duval B.P., Février O., Fil A., Galassi D., Havlickova E., Perek A. and Reimerdes H. 2019 SOLPS-ITER simulations of the TCV divertor upgrade
Plasma Phys. Control. Fusion **61** 085029
- [79] Février O. *et al* 2021 Divertor closure effects on the TCV boundary plasma
Nucl. Mater. Energy **27** 100977
- [80] Carr M. *et al* 2019 Physically principled reflection models applied to filtered camera imaging inversions in metal walled fusion machines
Rev. Sci. Instrum. **90** 043504
- [81] Carr M., Meakins A., Baciero A., Bernert M., Callarelli A., Field A., Giroud C., Harrison J., Hawkes N., Henderson S. and Lipschultz B. Towards integrated data analysis of divertor diagnostics with ray-tracing (Belfast, Northern Ireland UK June 26-30, 2017) 44th EPS Conf. Plasma Physics (European Physical Society)
- [82] Verhaegh K. *et al* (the TCV Team and the EURO fusion MST1 Team) 2021 The role of plasma-molecule interactions on power and particle balance during detachment on the TCV tokamak
Nucl. Fusion **61** 106014
- [83] Feng X. *et al* 2021 Development of an 11-channel multi wavelength imaging diagnostic for divertor plasmas in mast upgrade
Rev. Sci. Instrum. **92** 063510